

AFIT/GAE/ENY/95D-03

AN EXPERIMENTAL INVESTIGATION OF A
STING-MOUNTED FINITE
CIRCULATION CONTROL WING

Thesis

Lorenzo C. Bradley, Second Lieutenant, USAF

AFIT/GAE/ENY/95D-03

1996 0118 043

DTIC QUALITY INSPECTED 3

Approved for public release; distribution unlimited

The views expressed in this thesis are those of the author and do not reflect the official policy or position of the Department of Defense or the U.S. Government

AFIT/GAE/ENY/95D-03

AN EXPERIMENTAL INVESTIGATION OF A
STING-MOUNTED FINITE CIRCULATION CONTROL WING

THESIS

Presented to the Faculty of the School of Engineering
of the Air Force Institute of Technology
Air University

In Partial Fulfillment of the
Requirements for the Degree of
Master of Science in Aeronautical Engineering

Lorenzo C. Bradley III, B.S.
Second Lieutenant, USAF

December 1995

Approved for public release; distribution unlimited

Acknowledgments

I would like to thank all those that made this thesis possible. First, I would like to sincerely thank God. Only by His grace are all things possible. I am deeply indebted to Dr. Milton Franke, my thesis advisor, for challenging me with this project. His insight, guidance, and support during this experimental investigation made the ride much smoother. I would like to send special thanks to Mr. Tim Nathan, Mr. Dave Driscroll, and Mr. Jack Tiffany from the model shop. Their dedication to this project allowed me to continue following the numerous pitfalls.

This entire project would not have been possible without Mr. Charlie McNeely. His tireless dedication in providing technical support with instrumentation and wind tunnel operation enabled the completion of this project.

Most of all, I would like to thank my wife, Angela, for her patience, confidence, and support during this entire AFIT adventure. Her encouragement and motivation helped me get to the light at the end of that long dark tunnel.

Table of Contents

	Page
Acknowledgments.....	ii
List of Figures.....	v
List of Tables.....	vii
List of Symbols.....	viii
Abstract.....	xii
Chapter 1. Introduction.....	1
Chapter 2. Theory.....	5
Chapter 3. Test Item Description and Instrumentation.....	9
Wing Model.....	9
Blowing Air Supply System.....	14
AFIT 5-ft Wind Tunnel.....	15
Data Acquisition System and Force Balance.....	16
Chapter 4. Experimental Procedure.....	21
Calibration.....	21
Test Item Checkout.....	23
Preliminary Testing.....	24
Chapter 5. Data Reduction.....	26
Wind Tunnel Corrections.....	26
Lift Corrections.....	29
Drag Corrections.....	33
Equivalent Drag.....	34
Chapter 6. Results.....	37
Hysteresis Test.....	37
Repeatability Test.....	38

Clean Wing Configuration	38
Lift Coefficient	38
Equivalent Drag	41
Pitching Moment Coefficient	42
Comparison of Results to Previous Research	43
Comparison of Modified Wing Model Aerodynamic Data	46
Leading Edge Nose Droop	46
Leading Edge Nose Droop and Trailing Edge Splitter Plate	48
Wing Tip Fences	51
Lift Performance at Maximum Blowing	54
Equivalent Drag Performance at Maximum Blowing	55
Drag Polar	56
 Chapter 7. Conclusions	 58
 Chapter 8. Recommendations	 60
 References	 61
 Appendix A: Reduced Force Balance Data	 64
Hysteresis Test	74
Repeatability Test	75
 Appendix B: LabVIEW® Front Panel and Wiring Diagram	 76
 Appendix C: Data Uncertainty	 80
Data Acquisition System	80
Atmospheric Data Measurements	80
Force Balance and Wind Tunnel Measurements	80
Venturi Mass Flow Measurements	80
Center of Gravity Location	81
Overall Accuracy	81
 Vita	 82

List of Figures

Figure	Page
1. Planform View of Test Model	9
2. Detail of Blowing Slot, Coanda Surface and Trailing Edge Splitter Plate	10
3. Circulation Control Wing Cross-Section.....	11
4. Detail of Leading Edge Nose Droop.....	12
5. Detail of Wing Tip Fences	13
6. Schematic of Blowing Air Supply	14
7. Frontal View of the Wing Model Mounted on the Sting.....	19
8. Rear View of the Wing Model Mounted on the Sting	19
9. Venturi Mass Flow Apparatus in the Tunnel Control Room	20
10. Coordinate System for Six-Component Strain Gauge Balance	21
11. Jet Velocity Profile at the Trailing Edge	24
12. Effect of Air Supply Hoses on Lift Coefficient.....	29
13. Effect of Air Supply Hoses on Drag Coefficient.....	30
14. Hysteresis Results with LE Nose Droop	37
and TE Splitter Plate Configuration, $C_{\mu}=0.0$	
15. Repeatability Test with LE Nose Droop	38
and TE Splitter Plate Configuration, $C_{\mu}=0.0$	
16. Effect of Blowing on Lift Coefficient, Clean Wing Configuration.....	39
17. Effect of Blowing on Lift Coefficient, Clean Wing Configuration.....	39
18. Magnitude of Equivalent Drag Correction, Angle of Attack=0.0 deg	41

19. Effect of Blowing on Equivalent Drag Coefficient, Clean Wing Configuration	42
20. Effect of Blowing on Pitching Moment Coefficient, Clean Wing Configuration	43
21. Comparison of Lift Performance, Clean Wing and 180 deg TE Configuration	44
22. Comparison of Drag Performance, Clean Wing and 180 deg TE Configuration	45
23. Effect of Leading Edge Nose Droop on Stall Angle of Attack	46
24. Effect of Leading Edge Nose Droop on Pitching Moment Coefficient	47
25. Effect of Leading Edge Nose Droop on Equivalent Drag	48
26. Effect of Blowing on Lift Coefficient, LE Nose Droop and TE Splitter Plate Configuration	49
27. Effect of Trailing Edge Splitter Plate on Lift Coefficient	49
28. Effect of Trailing Edge Splitter Plate on Equivalent Drag Coefficient	50
29. Effect of Trailing Edge Splitter Plate on Pitching Moment Coefficient	51
30. Effect of Wing Tip Fences on Lift Coefficient, LE Nose Droop Configuration	52
31. Effect of Wing Tip Fences on Lift Coefficient, LE Nose Droop and TE Splitter Plate Configuration	52
32. Effect of Wing Tip Fences on Equivalent Drag, LE Nose Droop Configuration	53
33. Effect of Wing Tip Fences on Equivalent Drag, LE Nose Droop and TE Splitter Plate Configuration	54
34. Lift Performance at Maximum Blowing	54
35. Equivalent Drag Performance at Maximum Blowing	56
36. Drag Polar, Clean Wing and LE Nose Droop Configuration	57

List of Tables

Table	Page
1. Airfoil Geometry	10
2. Wing Parameters	12
3. Summary of Standard Wind Tunnel and Drag Corrections	29
4. Lift Coefficient Correction for Air Supply Tubes	31
5. Lift Coefficient Correction for Jet Thrust	32
6. Drag Coefficient Correction for Air Supply Hoses	34
7. Effect of Equivalent Drag Component on Drag Coefficient	36

List of Symbols

A	area	m^2
A_{base}	model base area	m^2
AR	aspect ratio	
b	wing span	cm
c	wing chord	cm
C_d	Venturi coefficient of discharge	
C_D	wing drag coefficient	
C_{Db}	bouyancy drag correction factor	
C_{Dbp}	base pressure drag correction factor	
C_{De}	wing equivalent drag coefficient	
C_{Di}	induced drag coefficient	
$C_{L\alpha}$	lift curve slope	
C_{Lmax}	maximum lift coefficient	
C_m	wing pitching coefficient about the model center of gravity	
C_μ	momentum coefficient	
C_{tunnel}	cross-sectional area of wind tunnel	m^2
D_e	equivalent drag	N
D_{meas}	drag measured during testing	N
F	force	N

g	acceleration of gravity	m/sec^2
h	trailing edge slot height	cm
KE	kinetic energy	J
dl	change in jet length	m
L	lift	N
LE	leading edge	
\dot{m}	mass flow rate	kg/sec
M	Mach number	
dp	change in static pressure	N/m^2
P	pressure	N/m^2
P_{atm}	atmospheric pressure	N/m^2
P_o	total pressure	N/m^2
P_{ts}	test section pressure	N/m^2
q	dynamic pressure	N/m^2
q_{org}	dynamic pressure calculated at the static pressure ports	N/m^2
dr	distance along a closed curve	
r	Coanda surface radius	cm
R	gas constant	$\text{J}/(\text{kg-K})$
Re	Reynolds number based on chord	
Re_{eff}	effective Reynolds number based on chord	
Re_{test}	test Reynolds number based on chord	
S	wing model planform area	m^2

T	temperature	K
T_{atm}	atmospheric temperature	K
TE	trailing edge	
T_o	total temperature	K
TF	turbulence factor	
V	velocity	m/sec
V_j	jet velocity of blowing air	m/sec
$\text{vol}_{\text{model}}$	wing model volume	m^3
WT	wing tip	
x	dimension rearward from wing leading edge	cm
z	airfoil dimension normal to the chord	cm

Greek Symbols

Δ	change	
γ	ratio of specific heats for air	
ρ	density of air	kg/m^3
μ	viscosity of air	$\text{N}\cdot\text{s}/\text{m}^2$
Θ	trailing edge angle	deg
Γ	circulation	m^3/sec

Subscripts

∞	freestream conditions
atm	atmospheric conditions
b	bouyancy

bp	base pressure
corr	corrected
De	equivalent drag
e	equivalent
eff	effective
i	induced
j	jet
meas	measured
o	total property
org	measured from the static pressure ports at the mouth of the tunnel
ts	test section
1	conditions upstream of Venturi
2	conditions at Venturi throat

Abstract

This study investigated the lift, drag and pitching moment performance of a circulation control wing in the AFIT 5-ft wind tunnel. The experimental wing model was a 20 percent thick, 8.5 percent camber, partial elliptical cross-section, single blowing slot, rectangular planform wing. The aspect ratios tested were 3.99, 3.77 and 3.75. The variables in the investigation included the slot blowing rate and model configuration. The model was modified by adding a leading edge nose droop, a trailing edge splitter plate and wing tip fences to improve flow at the leading edge, reduce separation effects, and encourage attached flow on the upper surface, respectively. Results showed increased lift due to the splitter plate at low blowing rates. The leading edge nose droop increased the stall angle of attack of the wing model as blowing was increased. The wing tip fences increased the lift coefficient at medium and high blowing rates.

AN EXPERIMENTAL INVESTIGATION OF A STING-MOUNTED FINITE CIRCULATION CONTROL WING

Chapter 1. Introduction

In recent years, considerable research has been conducted into the application of circulation control techniques to improve the vertical/short takeoff and landing (V/STOL) capabilities of fixed-wing aircraft. As aircraft cruise speeds increase, so do takeoff and landing speeds. This directly equates to increased runway lengths and increased stress and fatigue on aircraft landing gear.

V/STOL concepts have applications in both commercial and military operations. For civilian applications, they permit takeoff and landings on shorter runways and reduce the risk of an accident by decreasing the approach speed. They have greater climb and descent angles that reduce the noise footprint on the surrounding area. Military aircraft benefit from high-lift technology by operating from runways shortened by battle damage or improvised runways. Also, the steeper climb angle possible with V/STOL technology may be used to reduce the exposure time the aircraft is vulnerable to attack from the ground.

Currently, V/STOL techniques, such as vectored thrust and blown flaps, can produce high lift coefficients, but at the expense of complexity, weight, cost and power required. However, a more promising high-lift technique is the circulation control wing

that takes advantage of the Coanda effect. This effect allows a jet of air to remain attached to a curved surface due to a balance between the centrifugal forces in the jet and the pressure differential produced by the jet velocity (4:457). Typical two-dimensional circulation control airfoils have tripled the lift generation of the basic airfoil using a conventional mechanical flap (1:2).

Much research has been done in the area of circulation control airfoils. As early as 1967, Kind and Maull experimentally investigated the characteristics of a low speed circulation control elliptical airfoil and achieved lift coefficients greater than 3.0 (5:176). Englar, in his investigation of a cambered 30 percent thick circulation control airfoil produced lift coefficients up to 6.5 at moderate blowing momentum coefficients (2:1). One of the largest circulation control efforts was conducted by Englar et al. at the David W. Taylor Naval Ship Research and Development Center (6). This investigation included the flight test of an A-6A Intruder modified with a circulation control wing. The flight test generated increased lift and decreased landing speed, but at the expense of decreasing maximum speed.

Especially notable to this thesis was the work done by Stevenson, Franke, Rhynard, and Snyder (13) who investigated the effects of blowing rate and the trailing edge splitter plate on lift and drag at various angles of attack on a circulation controlled airfoil. Stevenson et al. found that the lift-to-drag ratio with the splitter plate was approximately double that for the clean configuration at low blowing rates. Also noteworthy to this investigation was the research conducted by Englar (24) who found that leading edge nose droop was an effective means of leading edge boundary layer

control. Englar found that as the droop angle increased, stall occurred at higher incidence due to the reduced leading edge separation.

Considerable research has been conducted at Wright-Patterson AFB, in the AFIT 5-ft wind tunnel. Harvell investigated dual-slot blowing (11), while Trainor (9) and Pelletier (10) developed testing methods. Lacher (8) established a limit on the maximum lift coefficient for a circulation control wing, and Tallarovic (7) tested various Coanda surfaces on a high aspect ratio circulation control wing.

The purpose of this investigation was to study a circulation control method using blowing for increasing the lift characteristics of a low-aspect ratio wing. Wind tunnel tests were conducted to determine the effects of the blowing rate and the effectiveness of the leading edge nose droop, splitter plate and wing tip fences on lift and drag at various angles of attack. Building upon the work of Tallarovic (7), this investigation tested a wing model modified to achieve higher lift coefficients. Testing took place in the AFIT 5-ft wind tunnel at a Reynolds number based on the wing chord of 5×10^5 . Force data was collected and reduced to coefficient form using a six-component 1.27 cm (0.5 in) balance and LabVIEW[®] data acquisition system.

Forthcoming in this report, the theory of circulation control will be discussed in Chapter 2. In Chapter 3, the wing model and the instrumentation of the experiment are reviewed. Next, the calibration of the instrumentation, the test item checkout, and the preliminary tests are described in Chapter 4. The wind tunnel, lift and drag corrections are listed in Chapter 5. The results of the investigation are discussed in Chapter 6. Finally, in

Chapters 7 and 8, the conclusions of this test and recommendations for further research are considered, respectively.

Chapter 2. Theory

For the purpose of clarity, it is necessary to briefly describe the fluid mechanics of circulation control wings. The Kutta-Joukowski theorem states that the force per unit span for a cylinder of arbitrary cross-section is equal to (15:47):

$$\vec{F} = \rho \vec{V} \times \vec{\Gamma} \quad (1)$$

where the circulation Γ is defined as the line integral of the velocity around any closed curve per unit span (20:69):

$$\Gamma = \oint_C \vec{V} \cdot d\vec{r} \quad (2)$$

Thus, the total lift for a wing of span, b , may be written as:

$$L = \rho_{\infty} V_{\infty} \Gamma b \quad (3)$$

and is directly related to the circulation about the wing. At lower airspeeds, lift can be maintained only by varying the density, the span of the wing or the circulation. Kohlman (16:123) states that, in practice, the most powerful method of maintaining lift at lower airspeeds is to increase circulation.

On an ordinary airfoil with a sharp trailing edge, the flow on the upper surface of the wing cannot turn around the trailing edge without separation unless the velocity is infinite. Since this is impossible, a restriction known as the Kutta condition is placed at the trailing edge. The Kutta condition states that

$$\Gamma(c) = 0 \quad (4)$$

and there exists a rear stagnation point ensuring that the velocity is finite and the flow leaves smoothly and tangentially from the trailing edge (15:45). For a given angle of attack of the airfoil, this departure at the trailing edge occurs for a particular value of circulation and, hence, a particular value of lift coefficient.

In contrast to a conventional airfoil, a circulation control airfoil has a rounded trailing edge and a jet of air is blown tangentially over the trailing edge Coanda surface. The Coanda effect allows for the adherence of the low pressure sheet of air to the Coanda surface due to a balance between the centrifugal forces in the jet and the pressure forces produced by the jet velocity. Consequently, the aft stagnation point moves to the lower surface increasing circulation and lift. The position of the stagnation points and the value of circulation are controlled by the magnitude of the blowing momentum coefficient, C_μ (16:163):

$$C_\mu \equiv \frac{\dot{m}_j V_j}{q_\infty S} \quad (5)$$

To calculate the momentum coefficient, it is necessary to calculate the mass flow rate of blowing air, the jet velocity, and the tunnel dynamic pressure. The mass flow rate was measured with a Venturi mass flow meter. According to Lacher (8), the mass flow rate for this investigation is:

$$\dot{m} = C_d A_2 P_1 \sqrt{\frac{2\gamma}{RT_1(\gamma-1)}} \sqrt{\frac{1 - (P_2 / P_1)^{\frac{\gamma-1}{\gamma}}}{(P_2 / P_1)^{\frac{2}{\gamma}} - (A_2 / A_1)}} \quad (6)$$

For the Venturi used in this test, $C_d = 0.970$, $A_2 = 0.000126 \text{ m}^2$ (0.001362 ft^2), $A_2/A_1 = 0.3677$, and P_1 and P_2 are the pressures read at the Venturi pressure taps.

The jet velocity is calculated assuming that the air within the wing expands isentropically through the blowing slot from the plenum total pressure to the free stream static pressure. Starting from the following relations:

$$\frac{T_o}{T} = 1 + \frac{\gamma - 1}{2} M^2 \quad (7)$$

$$\frac{P_o}{P} = \left[1 + \frac{\gamma - 1}{2} M^2 \right]^{\frac{\gamma}{\gamma - 1}} \quad (8)$$

$$M^2 = \frac{V^2}{\gamma R T} \quad (9)$$

the jet velocity may be written as:

$$V_j = \sqrt{2RT_o \left[\frac{\gamma}{\gamma - 1} \right] \left[1 - \left(\frac{P}{P_o} \right)^{\frac{\gamma - 1}{\gamma}} \right]} \quad (10)$$

where P_o is the total pressure in the wing plenum, and P is the pressure to which the air expands. T_o is the total temperature in the wing plenum. For the model checkout and the jet thrust runs where the wind tunnel is off, P is the atmospheric pressure. During the wind tunnel tests, the static pressure in the tunnel test section is the atmospheric pressure minus the corrected freestream dynamic pressure:

$$P_{ts} = P_{atm} - q_{\infty} \quad (11)$$

During the wind tunnel tests, the tunnel test section pressure was used to calculate the blowing coefficient instead of the local pressure at the velocity jet. According to Englar and Williams (23:12), at low blowing rates, where the plenum pressure is approximately equal to the test section pressure and $C_{\mu} \approx 0.0$, the local exit pressure is less than the test

section pressure. Using the local exit pressure would yield a more correct value of the blowing coefficient. The drawback to this approach is that the blowing coefficient would then be dependent on the local geometry external to the slot. This would not be convenient for comparing two models of different trailing edge geometries. The result would be different blowing coefficients for the same duct pressures and slot areas.

The tunnel dynamic pressure was calculated as follows:

$$q_{\infty} = \frac{(\text{Re } \mu)^2 RT_{atm}}{2P_{atm}c^2} \quad (12)$$

Substituting Equation (12), the test section pressure P_{ts} is:

$$P_{ts} = P_{atm} - \frac{(\text{Re } \mu)^2 RT_{atm}}{2P_{atm}c^2} \quad (13)$$

The Reynolds number based on the wing chord was calculated using the test section pressure. Prior to each test run, the atmospheric pressure was read from a mercury barometer and the atmospheric temperature was read from a mercury thermometer. Due to the capability of the LabVIEW® data acquisition system, for these tests, the Reynolds number and the tunnel dynamic pressure were held constant by the tunnel operator.

Chapter 3. Test Item Description and Instrumentation

Wing Model

The wing model used in this test was a 20 percent thick, 8.5 percent cambered, partial elliptic cross-section rectangular wing. The model consisted of a single trailing edge blowing slot separated in the center of the wing by the sting mounting block and two blowing air supply tubes as shown in Figure 1. Each half of the wing had a 22.86 cm (9 in) spanwise blowing slot adjusted to a height of 0.023 cm (0.009 in).

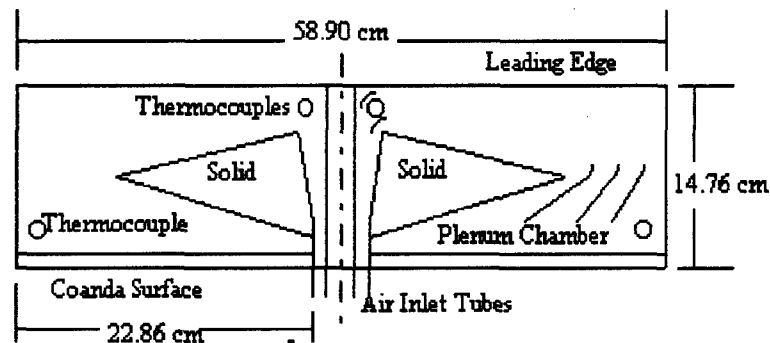


Figure 1. Planform View of Test Model

The blowing air was supplied by two 1.27 cm (0.5 in) i.d. hoses which were attached at the rear of the model on each side of the sting. The air supply hoses entered the wind tunnel downstream of the test section before attaching to the model. The interior of the model was designed as a diffuser to minimize pressure losses and reduce turbulence inside the model to achieve a uniform flow distribution across the trailing edge. Within the model, two air distribution tubes delivered air to the plenum chambers. As the air entered the model, the air was compressed as the area increased to prevent separation from the walls. Upon reaching the leading edge, guide vanes forced the air flow outward toward

the wing tips. The area of the duct increased outward and the air was diffused as it flowed forward (refer to Figure 1). Upon reaching the trailing edge, turning vanes were used to distribute the blowing air uniformly across the slot.

The height of the trailing edge slot and Coanda surface was designed according to Englar's research (1:3). Englar recommends a slot height to Coanda radius of $0.01 \leq h/r \leq 0.05$ for strongly attached Coanda turning and a Coanda radius to chord ratio of $0.02 \leq r/c \leq 0.05$ for effective jet turning and lift augmentation. The slot height was adjusted by means of 14 adjustment screws on the upper surface. The nominal slot height was 0.023 cm (0.009 in), providing a slot height to Coanda radius ratio of 0.028. The Coanda radius to chord ratio ranged from 0.052 to 0.055.

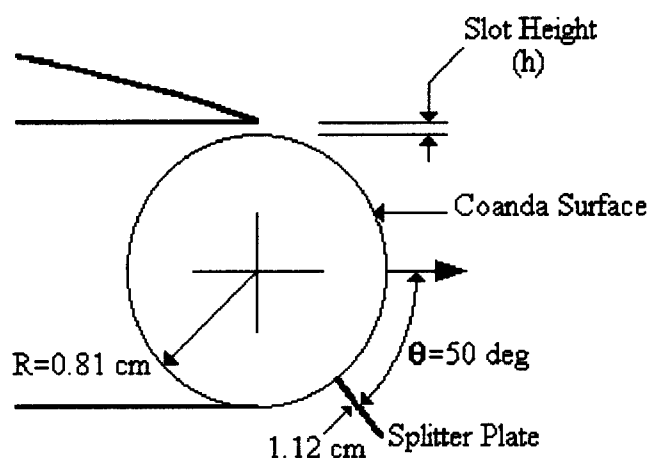


Figure 2. Detail of Blowing Slot, Coanda Surface and Trailing Edge Splitter Plate

The basic airfoil shape, shown in Figure 3, was similar to the model used by Tallarovic (7). The flat bottom of the plenum chamber was the wing lower skin, between

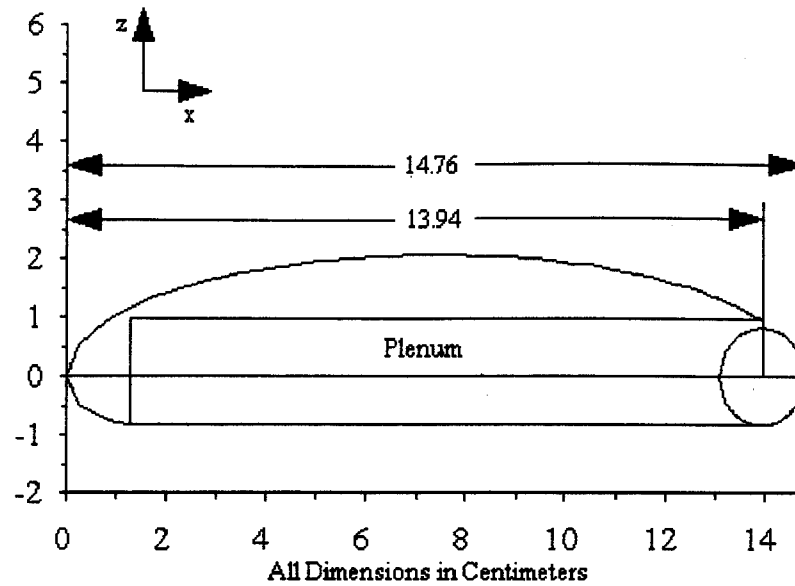


Figure 3. Circulation Control Wing Cross-Section

the nose of the model and the Coanda surface. The top of the model consisted of the top of the plenum chamber covered by a fiberglass skin. The airfoil geometry for the wing is provided in Table 1.

Table 1. Airfoil Geometry

Surface	Coordinate (cm)	Distance From Leading Edge (cm)
Upper	$z = 0.28\sqrt{((7.39)^2 - (7.39 - x)^2)}$	$0 \leq x \leq 13.94$
Lower	$z = -0.56\sqrt{((1.48)^2 - (1.48 - x)^2)}$	$0 \leq x \leq 1.48$
Lower	$z = -0.826$	$1.48 \leq x \leq 13.94$
Coanda Surface	$z = \pm\sqrt{((0.826)^2 - (x - 13.94)^2)}$	$13.94 \leq x \leq 14.76$

The basic airfoil shape was modified leading to five different model configurations, consisting of leading-edge nose droop, a trailing-edge splitter plate, and wing tip fences,

were tested in this experiment to improve circulation around the wing. The wing parameters for the configurations are listed in Table 2. With the maximum chord being 15.7 cm (6.18 in), the maximum chord to tunnel height ratio was 0.103. Wood (2:4)

Table 2. Wing Parameters

Model Configuration	Chord (cm)	Span (cm)	Planform Area (m ²)	Aspect Ratio
Clean Wing	14.76	58.90	0.087	3.99
w/ LE Nose Droop	15.70	58.90	0.092	3.77
w/ LE Nose Droop and Wing Tip Fences	15.70	59.06	0.093	3.75
w/ LE Nose Droop and TE Splitter Plate	15.70	58.90	0.092	3.77
w/ LE Nose Droop, TE Splitter Plate and Wing Tip Fences	15.70	59.06	0.093	3.75

suggests a maximum chord to tunnel height ratio of 0.25 to minimize interference caused by the constraint of the streamlines due to the ceiling and floor of the wind tunnel. The

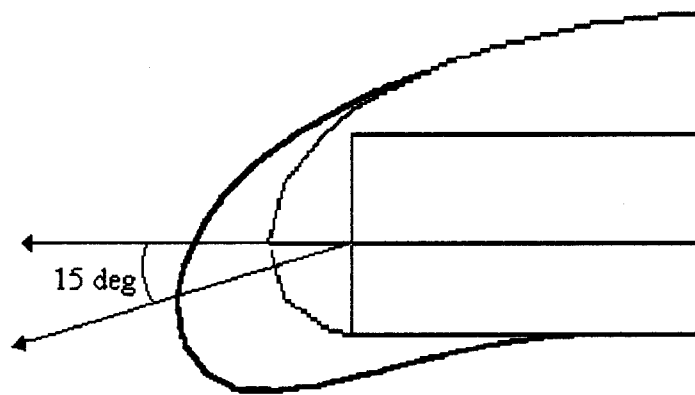


Figure 4. Detail of Leading Edge Nose Droop

conditions for this investigation were well within the specification stated by Wood.

The first variation to the basic model consisted of the addition of a nose droop (see Figure 4). Previous 2-D wind tunnel investigations by Englar (22:7) of a 15 percent thick elliptical airfoils indicated a problem with leading edge separation at high lift. A sharp pressure rise characteristic with local separation at the leading edge caused a decrease in the maximum lift coefficient at high angles of attack. For this investigation, a leading edge nose droop was incorporated to improve the flow at the leading edge and reduce suction on the upper surface of the leading edge. The nose droop was deflected 15 degrees from the centerline of the model. The addition of the nose droop increased the chord approximately 6 percent. The second modification was wing tip fences placed 2.54 cm (1 in) inboard of the right and left wing tip. The wing tip fences were used to encourage flow attachment on the upper surface. The wing tip fences had a uniform height of 1.27 cm (0.5 cm) around the outside of the model as shown in Figure 5. The addition of the

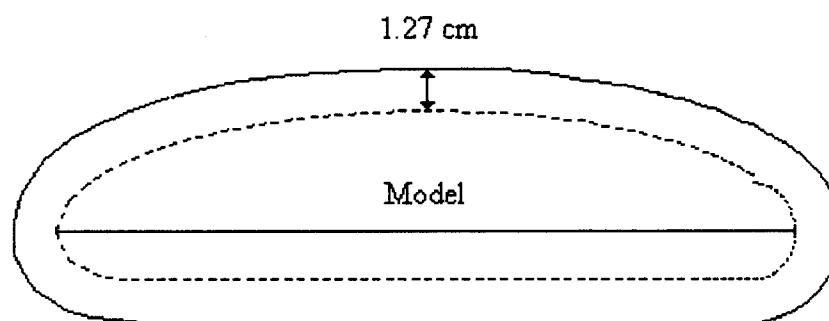


Figure 5. Detail of Wing Tip Fences

wing tip fences increased the planform area approximately 1 percent due to the thickness of the plate. The third modification was the splitter plate as shown in Figure 2. The splitter plate design on the Coanda surface was based upon flow visualization analysis and research done by Stevenson et al. (13:885). He achieved optimal lift to drag ratios with a

splitter plate chord to model chord ratio of 0.075 with a deflection of 45 degrees. The chord length of the splitter plate was 1.12 cm (0.44 in). Following tuft analysis, the splitter plate was located at $0.97 x/c$ and deflected 50 degrees from the centerline of the model.

Blowing Air Supply System

A schematic of the blowing air supply system is shown in Figure 6. The system consisted of a compressor, a 757.08 l (200 gal) tank, a compressed air dryer, and an

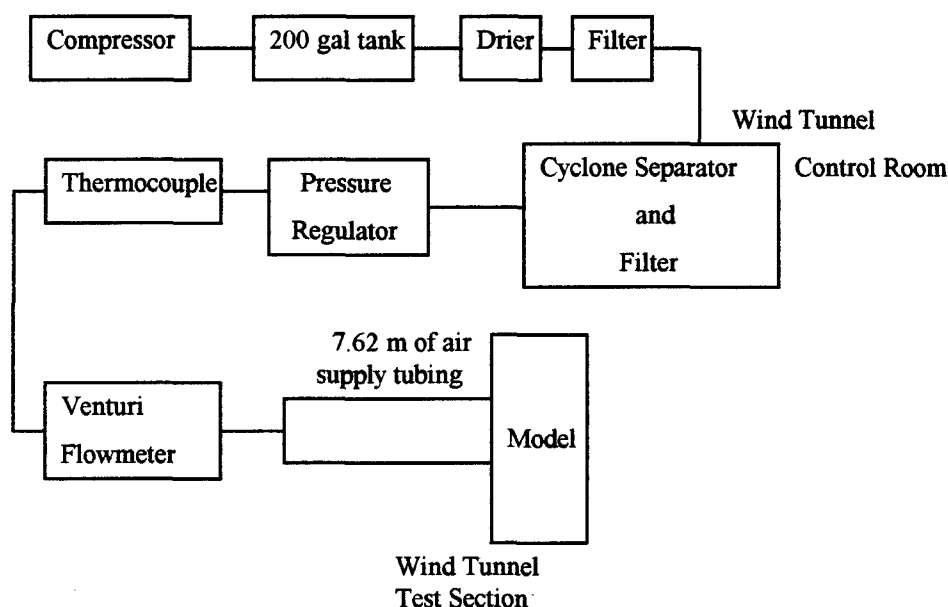


Figure 6. Schematic of Blowing Air Supply

in-line oil filter. Upon exiting the compressor, set to maintain 758 kPa (110 psig) \pm 20.69 kPa (3 psi) in the tank, the air flowed through the settling tank, drier and filter where it was then directed to the wind tunnel control room. Once in the control room, the compressed air flowed through a valve, cyclone separator and filter. Next, the air flow and model pressure were controlled by a regulator. A thermocouple and a Venturi mass flow meter were used to measure the mass flow rate of the air. Finally, the air was divided

into two streams and routed into the wind tunnel test section to pressurize both plena in the model. The Venturi mass flow apparatus is shown in Figure 9.

AFIT 5-ft Wind Tunnel

All testing was conducted in the AFIT 5-ft Wind Tunnel located in Building 19 of Area B at Wright-Patterson Air Force Base, Ohio. This wind tunnel is an open circuit tunnel with a closed test section enclosed in building designed to enhance flow circulation. The tunnel is capable of wind speeds up to 89 m/sec (293 ft/s) or 322 km/hr (200 mph) provided by two counter-rotating 3.66 m (12 ft) fans driven by four DC motors. The Reynolds number based on the wing chord for the circulation control tests was 5×10^5 , well below the maximum of 6.2×10^6 . The entrance of the tunnel has a contraction ratio of 3.7 to 1 and the test section is 1.52 m (5 ft) in diameter.

The tunnel total pressure is assumed to be atmospheric and static pressure is measured by a ring of eight static pressure ports located 0.76 m (2.5 ft) from the tunnel mouth and 3.4 m (11 ft) upstream of the tunnel test section. The static pressure ports are arranged in a ring from which the average static pressure was obtained as recommended by Rae and Pope (14:143). The tunnel dynamic pressure (tunnel q) is measured as the difference between the atmospheric pressure and the tunnel static pressure.

The wind tunnel has a turbulence factor of 1.5. This factor accounts for the effect of turbulence produced in the wind tunnel by the propeller, guide vanes, and the vibration of the tunnel walls. The effective Reynolds number is defined as the test Reynolds number multiplied by the turbulence factor and is used in comparing test results from different wind tunnels (14:147).

Data Acquisition System and Force Balance

The wind tunnel data acquisition system was controlled primarily by the LabVIEW® data acquisition system consisting of a data acquisition board and application software.

At the center of the data acquisition system was the AT-MIO-16(L) data acquisition card. The card had a 12 bit A/D converter and 16 analog inputs with data acquisition rates of up to 100 kHz. This highly accurate data card rejected noises as low as 0.1 LSB (least significant bit) rms with a typical differential non-linearity (DNL) of 0.5 LSB. In differential mode, where only 8 channels are available, each channel referenced its own ground signal. For this investigation, the data acquisition card operated in the differential mode to decrease the electrical noise in the environment. Each channel of the data card could be programmed to a particular gain, as specified in the user's manual (17). This feature allowed the user to maximize the precision of each channel by specifying the voltage range of the sampled data.

Data collected for the circulation control wing used the differential mode of the data acquisition card. Three cards were used to collect the data from 20 inputs, including voltages from the balance, thermocouples, pressure transducers, and horizontal sting (for angle of attack).

The LabVIEW® software is a program development application that uses the graphical programming language G to create programs in a block diagram format. The software package, when used with the data acquisition board, provided the user the capability to acquire, reduce and output data. From the front panel, the user controlled

the operation of the package with the controls, indicators and graphical outputs. The wiring diagram guided the signals coming from the data card along the wiring path to icons, equation blocks, or mathematical symbols to apply function to the signal. The results were displayed on the graphical outputs on the front panel (see Appendix B).

Forces and moments on the model were measured by an Able Corporation Mark V balance. The 1.27 cm (0.5 in) diameter, six-component, strain-gauge balance measures two normal forces of up to 890 N (200 lbf), two lateral forces of up to 445 N (100 lbf), one axial force of up to 222 N (50 lbf), and one rolling moment component of up to 4.5 N-m (40 in-lbf). Pitch and yaw moments were resolved by using the two normal and two side force measurements. Constant excitation voltage was provided by a Hewlett Packard 6205 regulated power supply. The Mark V balance was mounted on the end of a horizontal sting. The sting consisted of a "u" shaped yoke extending from the side walls of the tunnel with the sting extending from the center of the support as shown in Figure 8. The balance was designed to be inserted directly in the model where it was fastened with set screws from above and below the model.

A bank of Analog Devices 1B32AN Bridge Transducer Signal Conditioners was used in conjunction with the 6-component balance. These signal conditioning amplifiers were used to filter and boost voltage signals received from the balance. The amplifiers supplied the excitation voltage to the balance strain gages.

The angle of attack was determined from the voltage output of a position potentiometer connected to the sting. The voltage could be read from a Hewlett Packard

3466A digital multimeter and was recorded by the data acquisition card. The voltage was reduced to degrees by the data acquisition system software during tests.

The tunnel dynamic pressure was measured using a model 11234 Statham pressure transducer. Maximum pressure for the transducer was 103.4 kPa (15 psig). Model base pressure was measured with a Robinson-Halpern 0-25 inches of water pressure transducer. The right and left plenum total pressure and two Venturi flow meter pressure measurements were made using Endevco 8510B-100 pressure transducers powered by Endevco 4225 power supplies and conditioned with Endevco 4423 signal conditioners. The tunnel software resolved the voltages from the balance and pressure transducers into conventional aerodynamic coefficients displayed on the front panel.

Figures 7 and 8 show the front and rear view of the wing model mounted in the test section of the wind tunnel. In Figure 7 the 1.27 cm (0.5 in) air supply tubes are visible entering the tunnel test section and attaching to the rear of the model. The air supply hoses were tied along the yoke and the data acquisition lines were bundled and taped along the floor of the wind tunnel to reduce residual wake blockage and solid blockage effects.

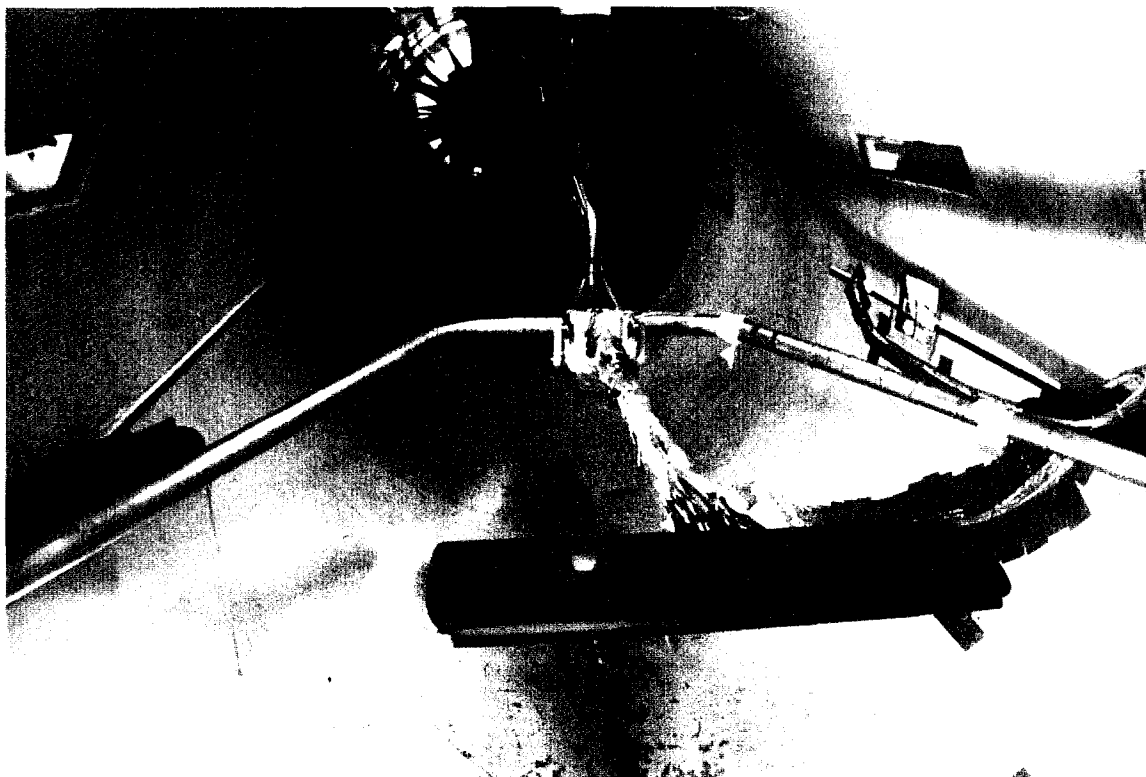


Figure 7. Frontal View of the Wing Model Mounted on the Sting

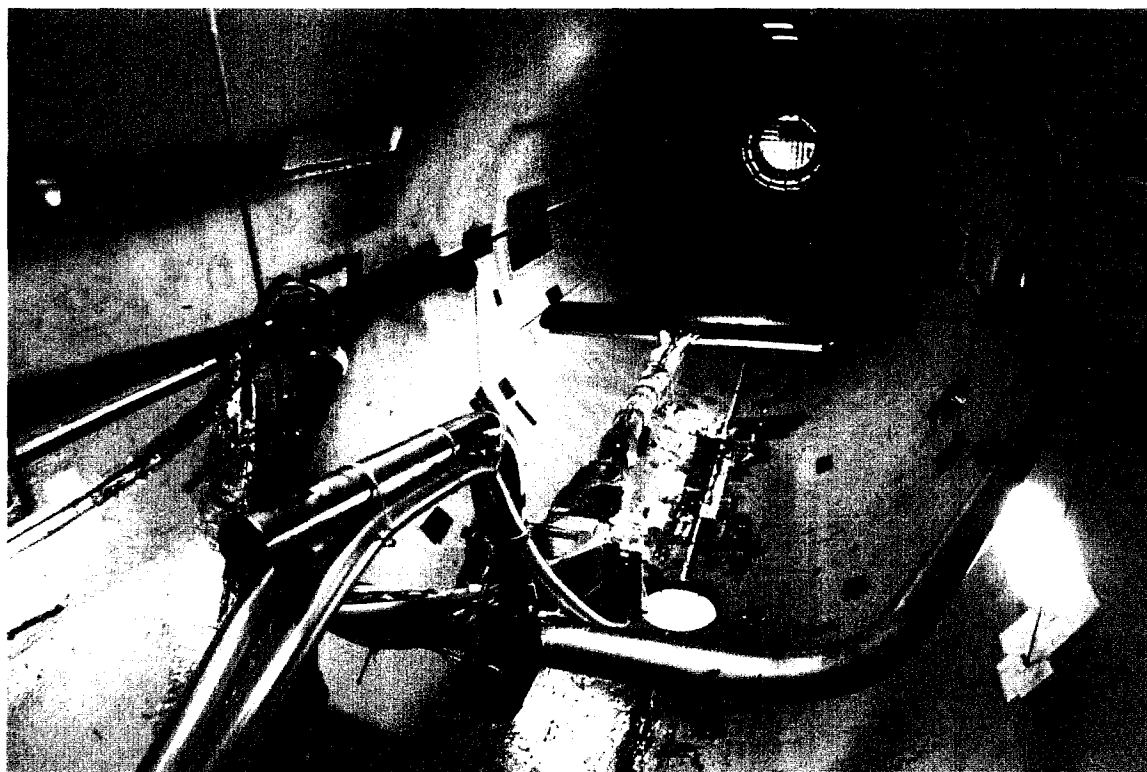


Figure 8. Rear View of the Wing Model Mounted on the Sting

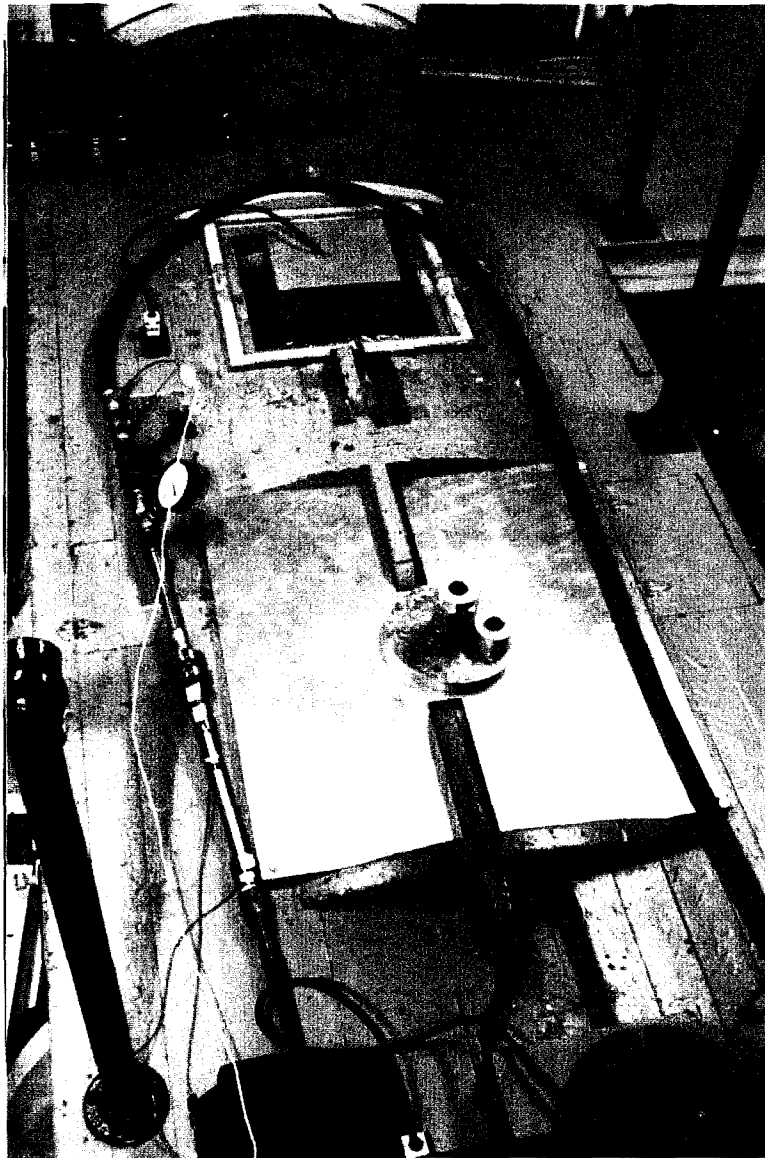


Figure 9. Venturi Mass Flow Apparatus in the Tunnel Control Room

Chapter 4. Experimental Procedure

Calibration

Several calibrations were conducted prior to testing. The force balance was calibrated prior to testing by applying known loads to each strain gauge. A calibration body and various loading apparatus were used to calibrate the balance. All of the strain gauges were loaded in the positive and negative directions of the balance's coordinate system except for the axial force gauge. Since only positive axial forces were expected,

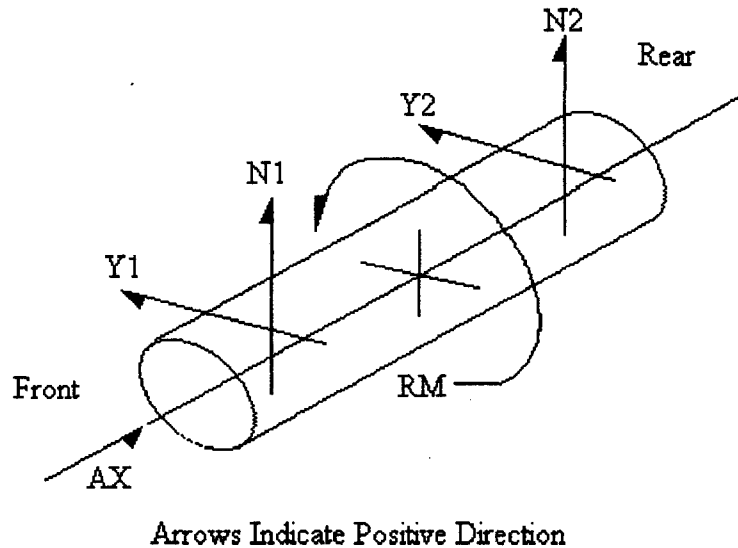


Figure 10. Coordinate System for Six-Component Strain Gauge Balance

the axial force gauge was only calibrated in the positive direction using a 13 point calibration from 0 to 266.9 N (60 lbf). Each normal force gauge was calibrated using a 13 point calibration from 0 to 266.9 N (60 lbf), each side force gauge was calibrated using a 11 point calibration from 0 to 222.4 N (50 lbf), and the rolling moment gauge was calibrated using a 11 point calibration from 0 to 44.48 N (10 lbf).

During the calibration of a single gauge, the data acquisition records all the strain gauge voltages, the excitation voltage, the weight, and the sting bend in minutes of angle. According to Rae and Pope, by measuring all six axis outputs due to the load on a single axis, balance interactions were determined (14:187). Upon completion of the calibration for each gauge, the calibration file was written and the linear fit of the calibration file was checked with the calibration curve correlation coefficient. All of the force gauges had a correlation coefficient of 0.9999 or greater. The 11 calibration files were combined to a single matrix which was used during testing to reduce the strain gauge voltages to forces and moments.

The pressure transducers were calibrated by applying a known pressure and recording the output voltage. The slope and intercept for the calibration of each transducer was determined by linear regression. The four Endevco pressure transducers were calibrated with an Ametek dead weight tester and Hewlett-Packard digital multimeter using 19 point calibrations. The Statham pressure transducer, used to measure tunnel dynamic pressure, and the Robinson-Halpern transducer, used to measure the base pressure, were also calibrated with an Ametek dead weight tester using 19 point calibrations. For all of the pressure transducers, the calibration curve correlation coefficient was 0.99999 or greater.

The angle of attack voltage from the sting was related to the wing angle of attack. The wing model was mounted on the sting with an inclinometer set on the model to measure angle of attack. The wing was set at set at angles of attack from -6 to 20 deg and

the voltage recorded. The angle of attack versus voltage curve was used by the data acquisition software to determine the wing angle of attack.

Test Item Checkout

Prior to installation in the wind tunnel, the model was checked for air leaks by installing the mass flow apparatus and attaching the two air supply tubes to the model. The model was pressurized by the blowing air with slot flow and checked for leaks by spreading leak detection fluid over seams and fastener holes. Leaks were sealed using wax and clay.

The jet velocity across the trailing edge was checked for uniformity. It was desired that the velocity and mass flow of blowing air from the slot be uniform across the span of the wing to achieve consistent performance during testing. The blowing slot was adjusted to a nominal height of 0.023 cm (0.009 in) using a feeler gauge. With the model mounted on a bench outside of the wind tunnel and the air supply hoses attached, a pitot probe was positioned in the jet of air exiting from the slot. Jet total pressure measurements were made in 1.27 cm (0.5 in) intervals along the span of the wing. In addition, the atmospheric pressure and plenum temperature were recorded. From these measurements, the jet velocity was calculated using Equation (10). Slot height was adjusted to achieve a relatively uniform velocity distribution across the span, however, the optimum jet velocity profile was achieved when the slot height was the same across the span. Figure 11 is an example of a jet velocity survey. As a result, when the model was in the wind tunnel the slot height needed to be checked. The maximum variation in jet velocity on any side was 16 percent.

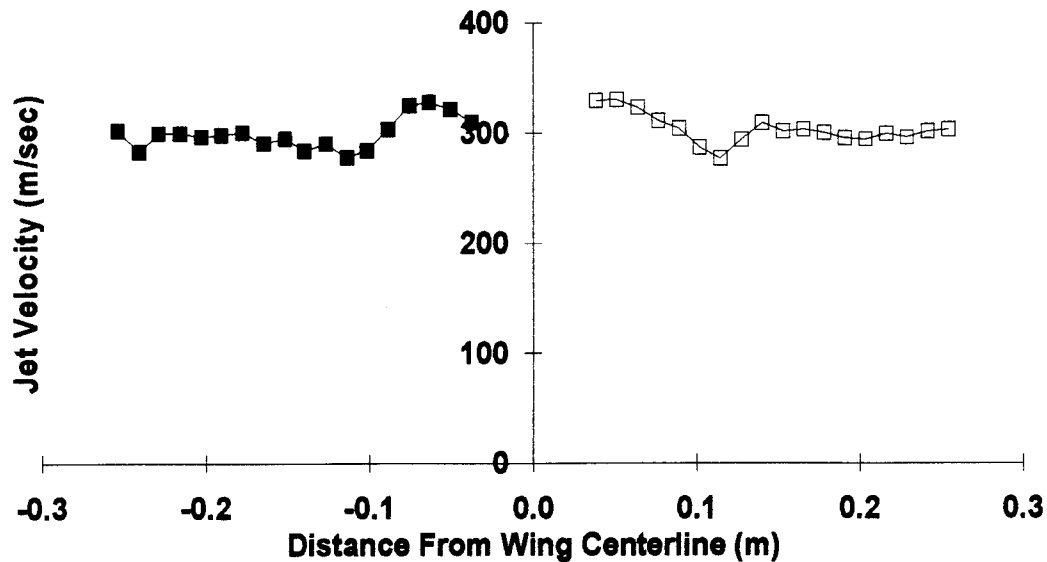


Figure 11. Jet Velocity Profile at the Trailing Edge

Once the model was installed in the wind tunnel and the data acquisition system connected, several tare runs were performed with the clean wing. The voltages and forces from the balance were recorded as the model moved through an angle of attack sweep ranging from -6 deg to 20 deg. This data would be used by the data acquisition system to eliminate the model weight from forces calculated during testing.

Preliminary Testing

In this test program, a test run was defined as several data acquisition points with a single parameter varied and all others held constant. A test run consisted of varying the angle of attack from -6 deg to 20 deg in 2 deg increments while holding the other parameters constant. The parameters varied include the model configuration and the mass flow rate of blowing air, represented by the blowing coefficient. The Reynolds number based on the wing model chord was approximately 5×10^5 for all of the tests.

Before the initial tare, a zero point was taken to account for any offsets and provide each run a reference starting point. Without the hoses attached, an initial tare and

test run were performed. Following another tare with the hoses attached, testing of the wing began. This procedure was done to isolate the effect of the hoses on the forces measured from the balance. Next, a test run was performed at the three values of blowing coefficient with the wind tunnel off to determine the thrust of the jet of air. This test was performed again with the tunnel on to isolate the contribution of the jet of air to the lift coefficient. The same procedure was followed for all of the model configurations being tested.

A hysteresis test was performed to determine variation in the voltage readings depending on whether the measured lift coefficient was approached from increasing or decreasing angle of attack. This variation could be caused by mechanical friction, magnetic effects, or thermal effects (18:7). All testing involved varying the angle of attack from -6 deg to 20 deg. For the hysteresis test, the angle of attack was decreased from 20 deg to -6 deg and compared to the previous run where the angle of attack was increased.

Chapter 5. Data Reduction

The wind tunnel data acquisition software automatically reduced the force balance strain gauge voltage outputs to forces. Weight tares were applied to eliminate the weight of the model. The software reduced the resulting forces into aerodynamic coefficients of lift, drag, and pitching moment about the center of gravity based on the corrected dynamic pressure and planform area of the model. These coefficients were reduced in the wind axis where lift is perpendicular and drag is parallel to the undisturbed flow.

Wind Tunnel Corrections

The LabVIEW[®] data acquisition software applied several standard wind tunnel corrections and drag corrections as recommended by Rae and Pope (14).

A skew factor of 1.019 was applied to the tunnel dynamic pressure (21). This factor accounts for the variance in the tunnel dynamic pressure calculated from the static ports at the mouth of the tunnel and the measured dynamic pressure in the test section. The relative magnitude of this correction for all test runs was 1.9 percent of the final value of the tunnel dynamic pressure.

Solid blockage is a correction for the volume of the model in the wind tunnel (14:353). The presence of the model forces the streamlines to curve around the model and squeeze together within the proximity of the tunnel walls. Subsequently, by continuity and the Bernoulli equation, the velocity of the flow and the dynamic pressure increase, hence, increasing the forces on the model.

Wake blockage is a correction that accounts for the flow in the wake moving slower than in the freestream (14:355). From continuity, the velocity of the flow outside

of the wake must be higher than the freestream to keep a constant volume or mass rate of flow of air passing through the test section. The higher velocity results in a lower pressure and an increased drag force.

The wake and solid blockage corrections were made to the tunnel dynamic pressure with the following equation:

$$q_{corr} = q \left(1 + \frac{k vol_{model}}{c_{tunnel}^{1.5}} + \frac{\alpha x for}{q 4 c_{tunnel}} \right)^2 \quad (14)$$

where q is the uncorrected dynamic pressure, k is the body shape factor, vol_{model} is the model volume, $\alpha x for$ is the measured axial force and c_{tunnel} is the cross-sectional area of the test section (14:365,367).

The buoyancy correction accounts for the decrease in cross-sectional area of the tunnel due to the thickening of the boundary layer along the tunnel walls. The result is a reduced pressure downstream and increased drag force (14:350). The buoyancy correction factor was obtained from the following equation:

$$C_{Db} = - \left(\frac{dp}{dl} \right) \frac{vol_{model}}{q_{corr} S} \quad (15)$$

where C_{Db} is the buoyancy drag coefficient, $\frac{dp}{dl}$ is the slope of the longitudinal static pressure curve where dp is the change in the static pressure and dl is the change in the jet length; vol_{model} is the volume of the model; q_{corr} is the corrected dynamic pressure, and S is the model reference area.

An induced drag correction accounts for the restriction of the streamlines, shed from an object in the freestream, by the tunnel walls (14:379). This drag correction factor

was obtained from the following equation:

$$C_{Di} = \frac{S}{8c_{tunnel}} C_L^2 \quad (16)$$

where C_{Di} is the induced drag coefficient, S is the model reference area, c_{tunnel} is the tunnel cross-sectional area, and C_L is the lift coefficient in the body axis. For this same phenomenon, a correction is made to the angle of attack using the following equation:

$$\alpha_{corr} = \alpha + 0.125 \frac{S}{c_{tunnel}} C_L \quad (17)$$

where α is the uncorrected angle of attack, S is the model reference area, c_{tunnel} is the tunnel cross-sectional area, and C_L is the lift coefficient in the stability axis.

The base pressure correction accounts for interference drag effect due to the connection between the model support and the model. This correction was obtained from the following equation (21):

$$C_{Dbp} = (P_{base} + q_{org}) \frac{A_{base}}{q_{corr} S} \quad (18)$$

where P_{base} is the base pressure at the sting mount, q_{org} is the upstream dynamic pressure from the static pressure ports, A_{base} is the model base area, q_{corr} is the corrected dynamic pressure, and S is the model reference area.

As shown by Lacher (8:48), these standard wind tunnel corrections are applicable to circulation control wings where the lift coefficient is less than four and the chord of the wing is less than 1/3 of the test section diameter. Listed in Table 3 is a summary of the standard wind tunnel and drag corrections in terms of percentage of final value. For each

Table 3. Summary of Standard Wind Tunnel and Drag Corrections

Angle of Attack = 4 deg, $C_{\mu} = 0$ Percentage of Final Value						
Wing Configuration	Solid Blockage	Wake Blockage	Buoyancy	Induced Drag	Base Pressure	Angle of Attack
Clean Wing	0.21	0.11	0.51	5.77	3.55	4.91
w/ LE Nose Droop	0.26	1.08	0.57	6.02	3.02	5.83
w/ LE Nose Droop and Wing Tip Fences	0.26	0.33	0.62	6.60	3.32	5.85
w/ LE Nose Droop and TE Splitter Plate	0.25	0.25	0.31	6.54	1.82	7.74
w/ LE Nose Droop, TE Splitter Plate and Wing Tip Fences	0.25	1.95	0.32	5.70	1.89	8.04

wing configuration, the corrections for the tunnel dynamic pressure were very small. The angle of attack correction was much larger in comparison and the drag coefficient corrections were less. Further corrections were made to the aerodynamic coefficients, including air supply hose and jet thrust corrections to the lift coefficient, and air supply hose and equivalent drag corrections to the drag coefficient.

Lift Coefficient Corrections

The first correction to the lift coefficient was for the effect of the air supply hoses attached to the model. This correction was obtained by plotting the lift coefficient versus angle of attack for the wing without and with the blowing hoses attached (see Figure 12).

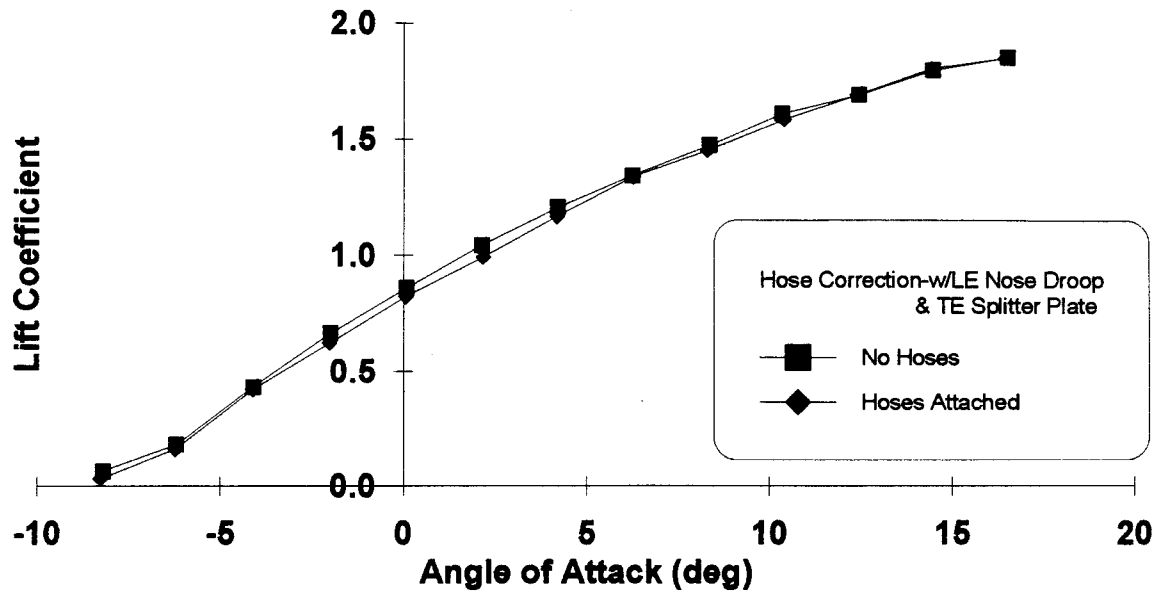


Figure 12. Effect of Air Supply Hoses on Lift Coefficient

Each lift curve was approximated with a second order polynomial of the form:

$$C_L = C_o\alpha^2 + C_1\alpha + C_2 \quad (19)$$

Since the two test runs were completed under identical conditions, the difference between the curves was due to the presence of the hoses. Hence, the correction for the air supply hoses was equivalent to the difference between the curves. The correction was calculated for every lift coefficient based on the corresponding angle of attack, and then added to all measured values of lift coefficient. This correction applied equally to all of the test configurations of the wing model. Table 4 shows the contribution of the hoses to the lift coefficient.

Table 4. Lift Coefficient Correction for Air Supply Hoses

$C_{\mu} = 0$, Modified Model with LE Nose Droop and TE Splitter Plate

Angle of Attack (deg)	Percentage of Final Value
0.06	3.94
2.17	3.33
4.20	2.79
6.27	2.32
8.30	1.97
10.40	1.57
12.40	1.20
14.44	0.81
16.44	0.42

As the angle of attack increased and, subsequently, the lift coefficient increased, the correction for the hoses decreased.

The second correction to the lift coefficient was for the lift component caused by the thrust from the jet of blowing air. For each model configuration, an angle of attack sweep was completed with the wind tunnel off. The momentum coefficient was varied for each alpha sweep. The data acquisition system recorded the forces on the balance caused by the blowing air and reduced the forces to lift coefficient form. The model was later tested at the same values of momentum coefficient with the wind tunnel running. Then, during data reduction, the lift coefficient, with the tunnel running, was corrected for the jet thrust by subtracting the lift coefficient caused by the blowing air. The jet thrust corrections are summarized in Table 5.

Table 5. Lift Coefficient Correction for Jet Thrust

Angle of Attack = 0 deg

Wing Configuration		Magnitude of C_L Correction	Percentage of Final Value
Clean Wing	Low Blowing	0.011	0.83
	Medium Blowing	0.026	1.25
w/ LE Nose Droop	Low Blowing	0.012	0.91
	Medium Blowing	0.039	1.77
	High Blowing	0.069	2.85
w/ LE Nose Droop and Wing Tip Fences	Low Blowing	0.015	0.84
	Medium Blowing	0.036	1.61
	High Blowing	0.045	1.67
w/ LE Nose Droop and TE Splitter Plate	Low Blowing	0.034	1.97
	Medium Blowing	0.096	4.93
	High Blowing	0.174	8.65
w/ LE Nose Droop, TE Splitter Plate and Wing Tip Fences	Low Blowing	0.033	1.92
	Medium Blowing	0.095	4.69
	High Blowing	0.176	8.09

The jet thrust correction was a function of both the blowing momentum coefficient and the model configuration. At all levels of blowing, the jet thrust correction was smallest with the clean wing configuration and the largest with the LE nose droop and TE splitter plate configuration. In comparing the configurations with the wing tip fences, although the correction was similar at medium and high blowing rates, the lift correction decreased in percentage of final value. This trend is due to the increased lift coefficients achieved at these blowing rates with the tip fences.

The addition of the splitter plate increased the magnitude of the lift correction. The percentage increase at the medium and higher blowing rates was caused by lower

lift coefficients due to premature flow separation on the Coanda surface.

Drag Coefficient Corrections

The drag coefficient was corrected for the air supply hoses in the same manner as the lift coefficient. The drag coefficient was plotted versus angle of attack without and then with the hoses attached, Figure 13. The drag coefficient correction for the hoses was

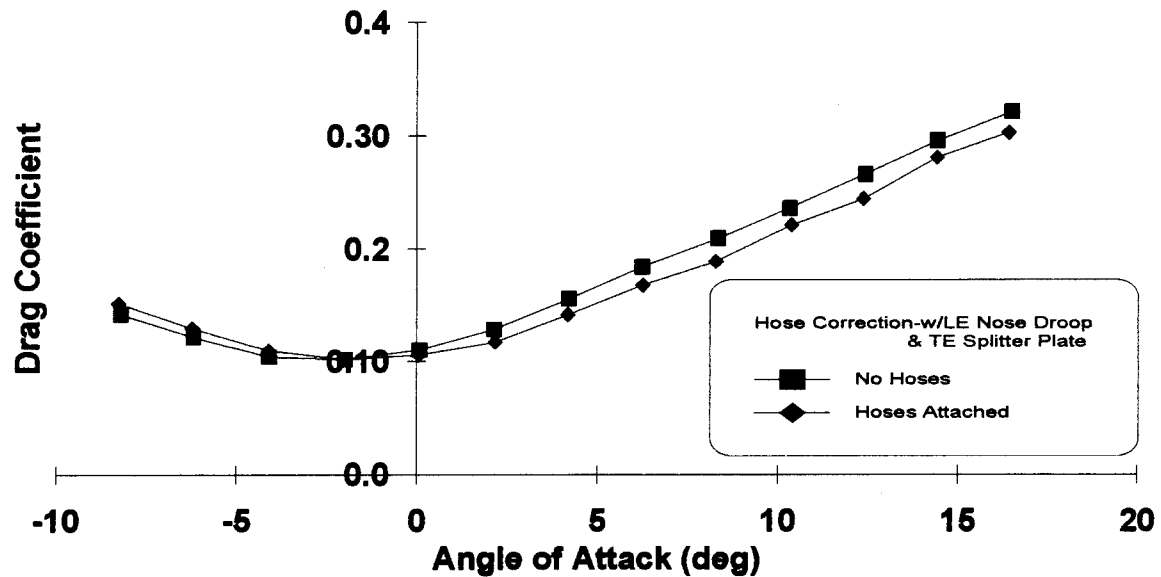


Figure 13. Effect of Air Supply Hoses on Drag Coefficient

equivalent to the difference between the two curves. From the figure, the air supply hoses caused a reduction in the measured drag coefficient. In comparison to the lift coefficient correction, Tallarovic (25:7) states that the lift loads tend to bend the hoses, where the drag loads compress the hoses axially. The reduction of drag caused by the hoses indicates that the hoses were much more rigid axially leading to higher hose corrections to the drag coefficient.

The drag correction was of the form:

$$C_D = C_o \alpha^2 + C_1 \alpha + C_2 \quad (20)$$

The correction was calculated for each drag coefficient based on the corresponding angle of attack and then added to all measured values of drag coefficient. Table 6 shows the contribution of the hoses to the drag coefficient.

Table 6. Drag Coefficient Correction for Air Supply Hoses

$C_{\mu} = 0$, Modified Model with LE Nose Droop and TE Splitter Plate

Angle of Attack (deg)	Percentage of Final Value
0.06	2.91
2.17	6.17
4.20	7.54
6.27	8.14
8.30	8.52
10.40	8.15
12.40	7.93
14.44	7.19
16.44	6.77

This correction applied equally to all of the test configurations of the wing model.

Equivalent Drag

Blown wing performance is presented in terms of equivalent drag. The equivalent drag is used as a direct comparison with the efficiencies of conventional wings. It takes into account the energy expenditures necessary to produce the blowing. The first term of Equation (21) accounts for the measured drag. The second term accounts for the engine power, most likely in the form of compressor bleed air, required to produce the blowing. In addition, the equivalent drag accounts for the thrust caused by the jet of air exiting the wing, the third term of Equation (21). As shown by Englar (2:15), the equivalent drag is written as:

$$D_e = D_{meas} + \frac{\Delta KE}{V_\infty \Delta t} + \dot{m} V_\infty \quad (21)$$

$$D_e = D_{meas} + \frac{\dot{m} V_j^2}{2 V_\infty} + \dot{m} V_\infty \quad (22)$$

or in coefficient form:

$$C_{De} = C_D + C_\mu \frac{V_j}{2 V_\infty} + C_\mu \frac{V_\infty}{V_j} \quad (23)$$

The freestream velocity was calculated using the Bernoulli equation and the equation of state:

$$q_\infty = \frac{\rho V_\infty^2}{2} \quad (24)$$

$$P_\infty = \rho_\infty R T_\infty = P_{atm} - q_\infty \quad (25)$$

where P_∞ is the test section pressure P_{ts} . Using Equation (24), the freestream velocity can be written as:

$$V_\infty = \sqrt{\frac{2 q_\infty R T_{atm}}{P_{atm} - q_\infty}} \quad (26)$$

Table 7 is a summary of the equivalent drag correction subject to circulation control airfoils. The magnitude of the equivalent drag correction, shown in the third column, is the sum of the second and third terms of Equation (23). The fourth column, the percentage of final value, is the percent-wise effect of these two terms on the total equivalent drag calculated from Equation (23).

Table 7. Effect of Equivalent Drag Component on Drag Coefficient

Angle of Attack = 0 deg

Wing Configuration		Magnitude of Equivalent Drag Correction	Percentage of Final Value
Clean Wing	Low Blowing	0.13	53.02
	Medium Blowing	0.50	64.36
w/ LE Nose Droop	Low Blowing	0.11	59.30
	Medium Blowing	0.45	72.19
	High Blowing	0.96	80.18
w/ LE Nose Droop and Wing Tip Fences	Low Blowing	0.11	61.39
	Medium Blowing	0.47	69.56
	High Blowing	0.97	80.30
w/ LE Nose Droop and TE Splitter Plate	Low Blowing	0.12	41.39
	Medium Blowing	0.50	77.61
	High Blowing	0.95	87.44
w/ LE Nose Droop, TE Splitter Plate and Wing Tip Fences	Low Blowing	0.12	41.49
	Medium Blowing	0.45	73.50
	High Blowing	0.96	89.07

In each case, the energy expenditure of blowing air had a significant effect on the total drag of the wing. In cases where the magnitude of the equivalent drag contribution was similar, while varying in the configuration, the difference in the percentage of final value was attributable to the higher or lower value of the drag coefficient. For a further examination of these values, refer to the results shown in the next chapter.

Chapter 6. Results

Hysteresis Test

As mentioned in the experimental procedure section, a hysteresis test was performed prior to testing. The results of the hysteresis test are shown in Figure 14.

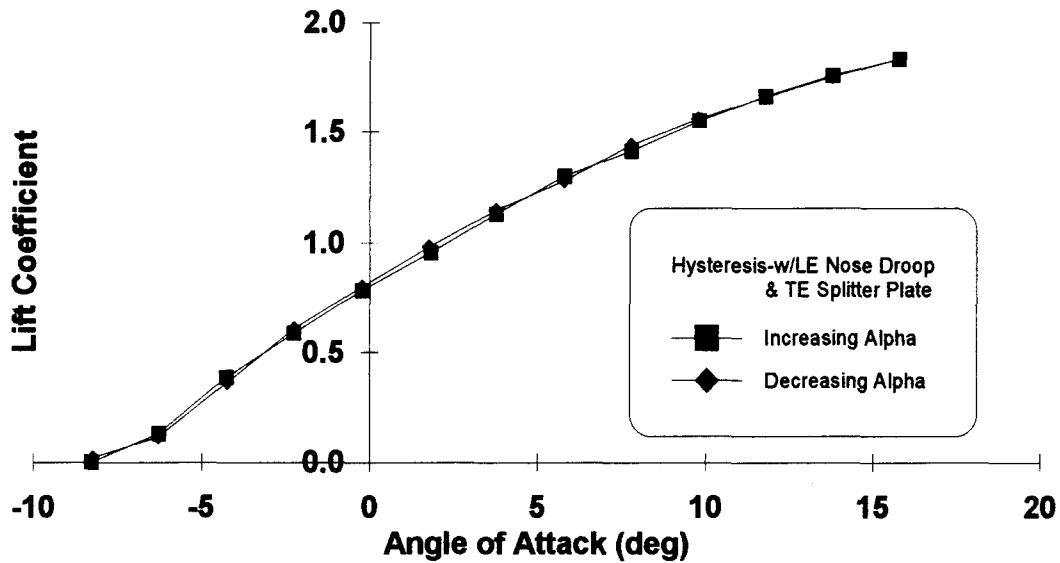


Figure 14. Hysteresis Results with LE Nose Droop and TE Splitter Plate Configuration, $C_{\mu}=0.0$

The results show that at the higher angles of attack, there was little indication of hysteresis in the balance strain gauges. The maximum difference between the two curves was small, on the order of 0.03, and occurred at approximately 2 deg angle of attack. Expressed in terms of percent of lift coefficient, this difference was on the order of 2.9 percent at the corresponding angle of attack.

Repeatability Test

A repeatability test was performed to determine that the measured values were recurrent under identical conditions. This test was conducted by measuring values at points from an earlier test. The results of the repeatability test are shown in Figure 15.

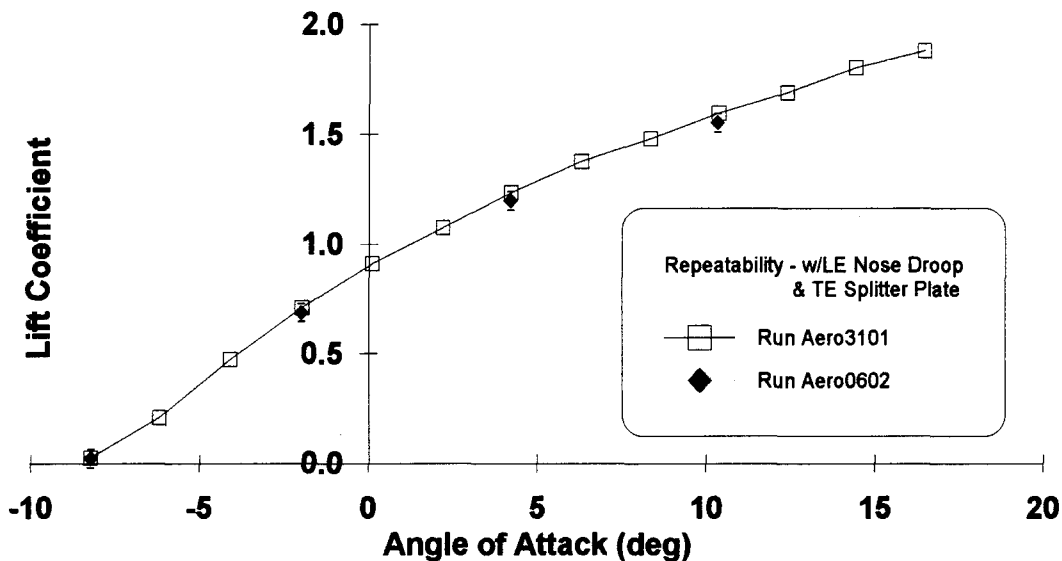


Figure 15. Repeatability Test with LE Nose Droop and TE Splitter Plate Configuration, $C_{\mu}=0.0$

The results suggest a high degree of repeatability. At the same angle of attack, the maximum difference between the measured lift coefficient of the two tests was 0.04. This corresponded to an error of 2.7 percent at the corresponding angle of attack.

The results of the hysteresis and repeatability tests show deviation in the data of less than 3 percent. These results are within the determined overall accuracy of the data of this investigation as stated in Appendix C.

Clean Wing Configuration

Lift Coefficient The clean wing configuration consisted of the unmodified wing model. The lift results of this test are presented in Figure 16. The results show that as the

blowing rate increased, the lift coefficient increased at a fixed angle of attack. However,

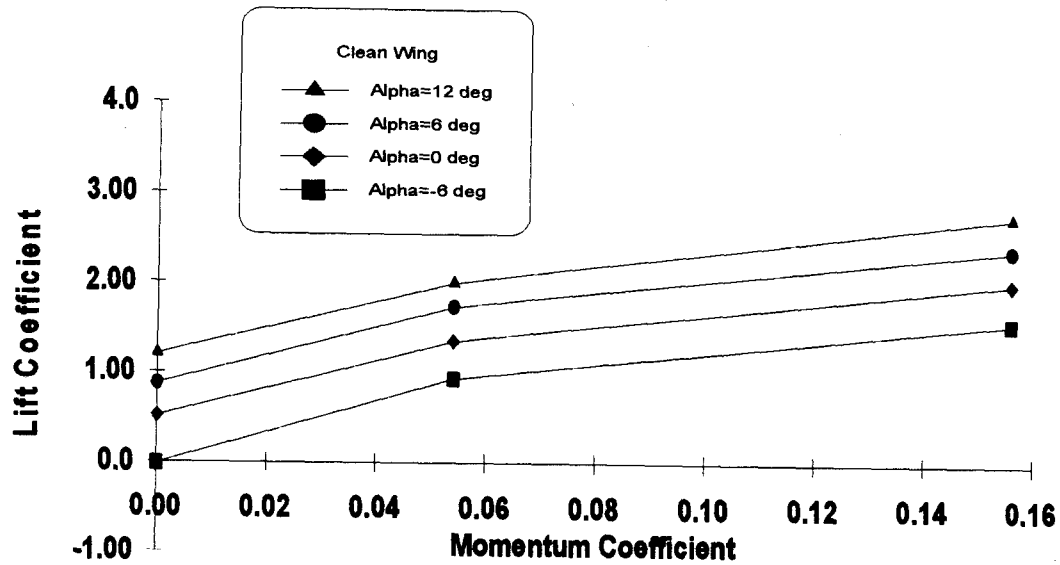


Figure 16. Effect of Blowing on Lift Coefficient, Clean Wing Configuration

at a given angle of attack, the slope of the C_L vs. C_{μ} curve decreased as the blowing rate increased. This is indicative of a limit on circulation-induced lift.

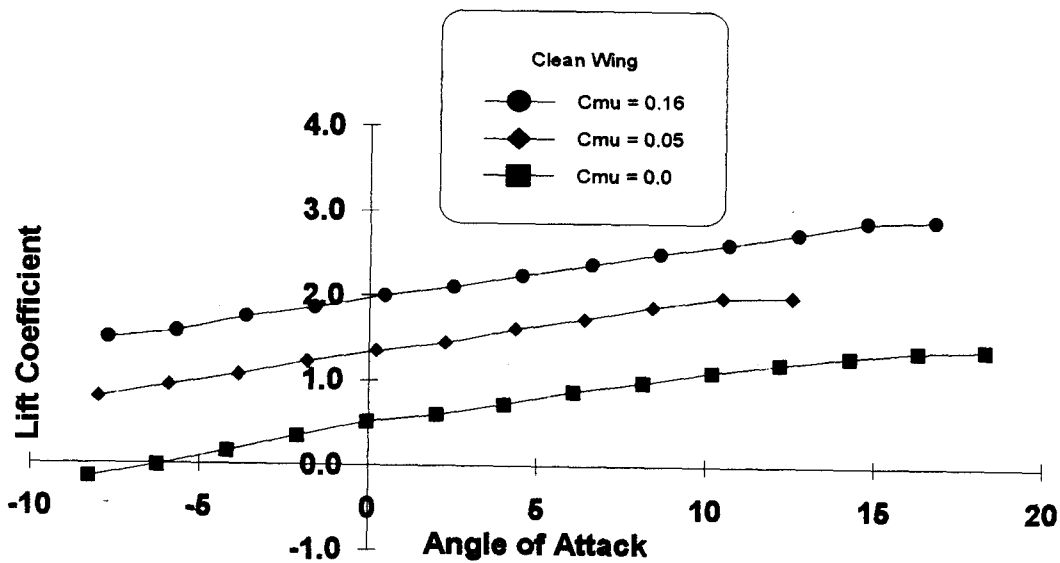


Figure 17. Effect of Blowing on Lift Coefficient, Clean Wing Configuration

The effect of blowing in terms of the lift coefficient versus angle of attack is shown in Figure 17. Due to the increase in the blowing rate, the C_L vs. α curve was shifted up. Also, the slopes of the C_L vs. α curve were constant at 0.06 per deg for each blowing rate. With regards to the slopes, basic lifting line theory assumes that the effect of aspect ratio on the lift curve slope for an elliptic wing loading with undeflected vortex sheet is given by the equation (15:70):

$$C_{L\alpha} = \frac{2\pi AR}{AR + 2} \quad (27)$$

For this configuration, where aspect ratio was 3.99, this equation corresponded to a lift curve slope of 0.073 per deg (1.33π per rad) as opposed to 0.11 per deg (2π per rad) for a wing of infinite aspect ratio. McCormick (15:70) offers a first-order correction to lifting line theory for large aspect ratio wings as:

$$C_{L\alpha} = \frac{2\pi AR}{AR + 2(AR + 4)/(AR + 2)} \quad (28)$$

Using this equation, the lift curve slope was 0.066 per deg (1.20π per rad). The agreement between the measured value and the predicted value was within 10 percent, somewhat validating the experimental results for the non-blowing case. By applying corrections to Equation (28) for a rectangular wing loading, improved agreement may be obtained.

From Figure 17, the increased blowing rate shifted the stall angle of attack. At $C_u=0.05$, the stall angle of attack decreased from 18.3 deg to 12.5 deg. This trend is not unusual. McCormick (15:173) shows that as the $C_{L_{max}}$ increases the stall angle of attack decreases for airfoil-trailing edge flap configurations. In comparison to Englar (22:28),

using a 15 percent thick circulation control airfoil with a slot height of 0.025 cm (0.01 in), the stall angle of attack decreased approximately 4 deg from $C_{\mu}=0.0$ to $C_{\mu}=0.06$. At $C_{\mu}=0.16$, the stall angle of attack increased to 16.8 deg (reference Figure 17). A tuft flow visualization test revealed that the decreased stall angle of attack was caused by the disruption of the flow of air around the trailing edge at low blowing rates leading to early separation. At higher blowing rates, the air flow was energized and remained attached to the Coanda surface at higher angles of attack resulting in an increased stall angle of attack.

Equivalent Drag. The equivalent drag coefficient is used when comparing the performance of circulation control wings with conventional wings. It accounts for the engine power necessary to produce blowing as well as the thrust caused by the velocity jet. These factors are a substantial portion of the total drag. For the purposes of this investigation, where blowing air was used, the equivalent drag coefficient of Equation (23) was the total drag coefficient.

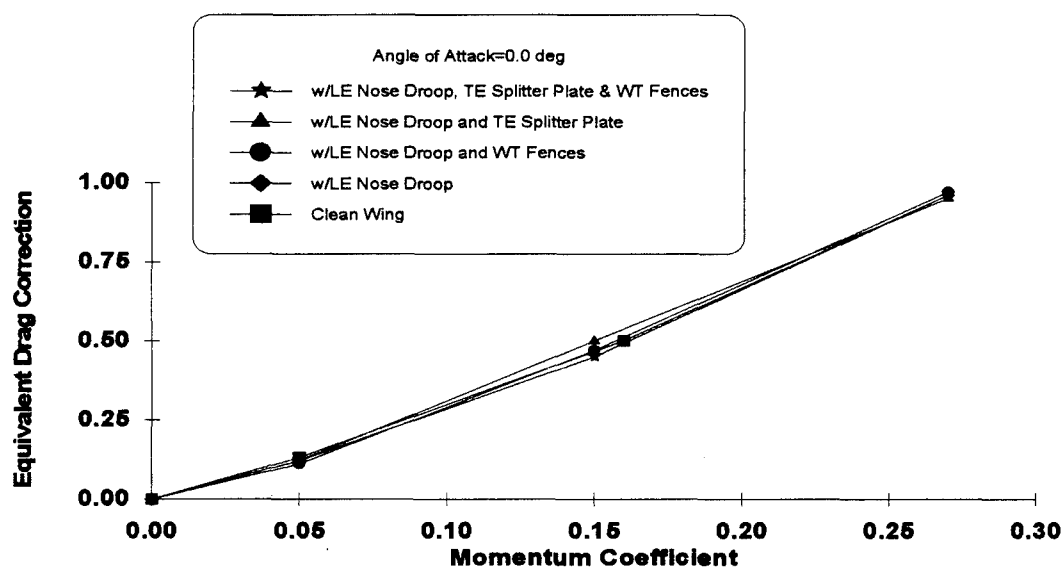


Figure 18. Magnitude of Equivalent Drag Correction, Angle of Attack=0 deg

Figure 18 shows the magnitude of the equivalent drag correction to the total drag against the blowing rates. For each configuration, the increase in the drag coefficient was approximately of equal magnitude. This is due to the fact that the last two terms of Equation (23) are only dependent on the blowing rate, freestream velocity, and jet velocity. Hence, since all of these configurations were tested under similar conditions to compare performance, i.e. similar blowing rate, freestream velocity, and jet velocity, the magnitude of the correction was equal for all of the configurations.

Figure 19 shows the increase in the equivalent drag coefficient as blowing rate increased for the clean wing configuration. The increase in the equivalent drag coefficient was representative of the increase in the drag correction as shown in Figure 18.

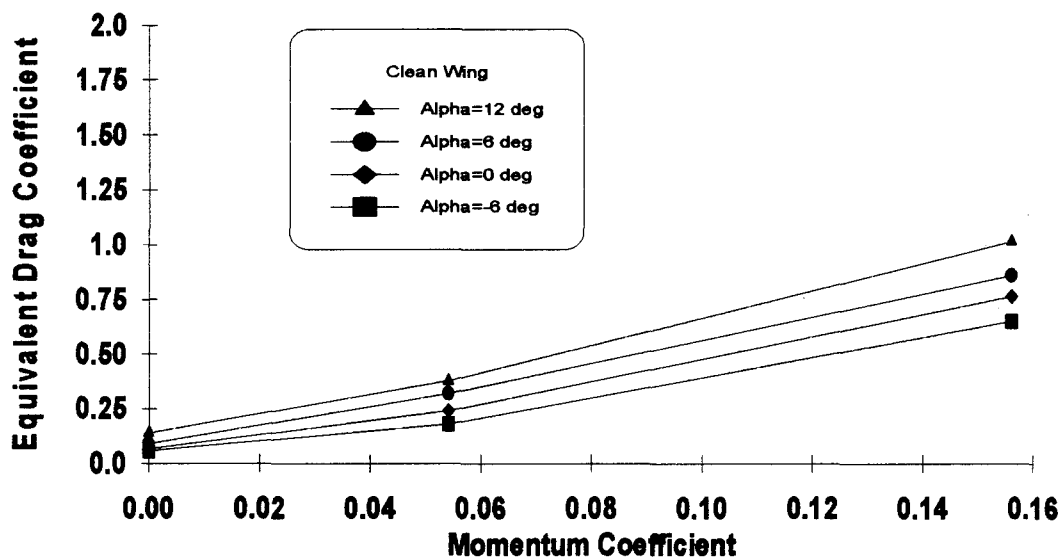


Figure 19. Effect of Blowing on Equivalent Drag Coefficient, Clean Wing Configuration

Pitching Moment Coefficient. According to Englar (22:10), a characteristic of tangentially blown airfoils is an increased suction region near the trailing edge which generates increased nose down pitching moments. Figure 20 shows the pitching moment about the model center of gravity versus the blowing coefficient.

The results show a decrease in the pitching moment as the blowing coefficient was increased for a given angle of attack. This trend is characteristic of an increasing nose down pitching moment as the blowing is increased. At 6 deg angle of attack, the positive lift was acting in front of the center of gravity producing a positive pitching moment. However, increased tangential blowing created a lift contribution aft of the center of

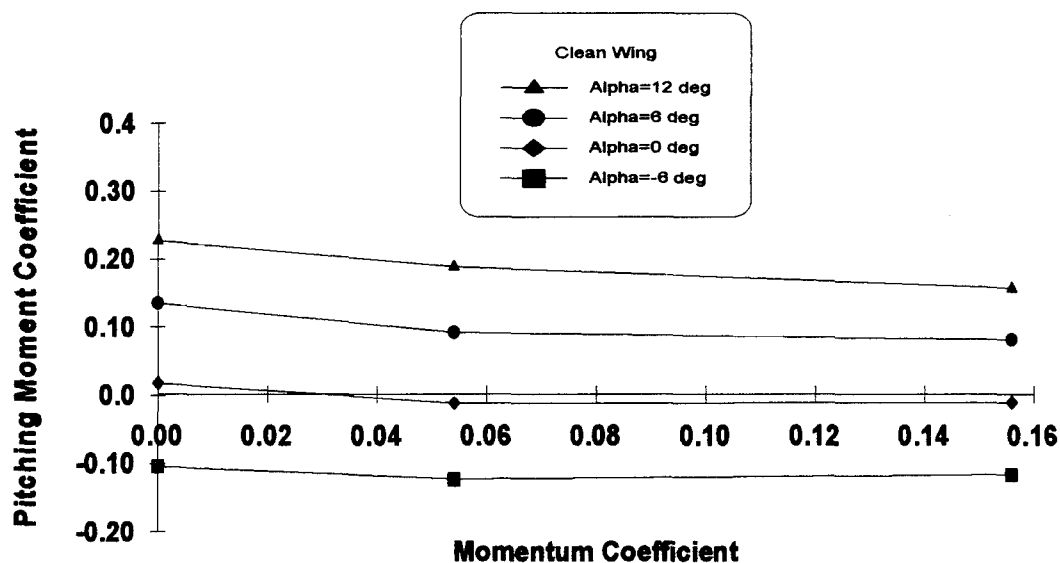


Figure 20. Effect of Blowing on Pitching Moment Coefficient, Clean Wing Configuration. As the blowing coefficient increases, the pitching moment coefficient decreases for all angles of attack. At 0 deg angle of attack, the decreasing pitching moment was due entirely to blowing, whereas at -6 deg angle of attack, the effects of the incidence and blowing were additive and caused larger negative pitching moment coefficients about the center of gravity (12:7). The nose down pitching moment was decreased as the angle of attack was increased.

Comparison of Results to Previous Research

As mentioned in the introduction, this experimental investigation built upon the work of Tallarovic (7). The variables in his research included the blowing rate and three differently shaped trailing edge Coanda surfaces. With the 180 deg trailing edge attached

to the wing model, the clean wing configuration from this investigation was similar in cross-section and aspect ratio. The Reynolds number based on the model chord for his research was 5×10^5 . Using Tallarovic's 180 deg trailing edge results, the lift and drag results are compared to those of the clean wing configuration from this investigation in Figures 21 and 22.

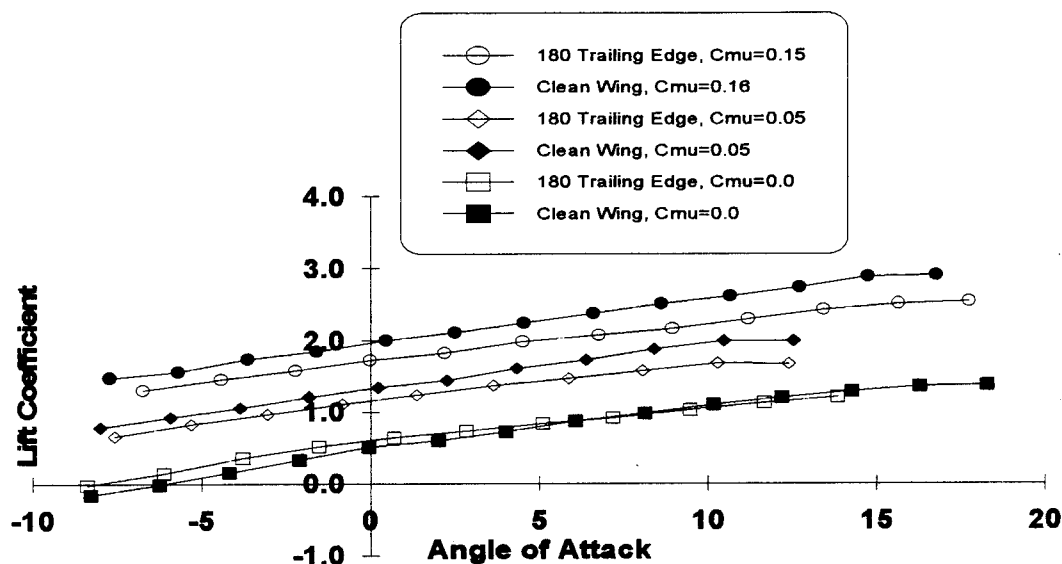


Figure 21. Comparison of Lift Performance, Clean Wing and 180 deg TE Configuration

In comparison of the lift performance, the slopes of the lift coefficient vs. alpha curves were constant at 0.06. At $C_{\mu}=0.0$, the difference between the curves is on the order of 0.01 at higher angles of attack. At $C_{\mu}=0.05$, the difference was on the order of 0.12 and at $C_{\mu}=0.16$, the difference was approximately 0.19. The stall angles of attack for the medium and high blowing rates were similar for the two configurations.

With respect to the maximum lift coefficient, one objective of Tallarovic's investigation was to achieve lift coefficients as high as the theoretical limits as stated by

McCormick (15:56, 64). Offered as a departure from lifting line theory to account for the deflected vortex sheet, the maximum lift coefficient is given as:

$$C_{L_{\max}} = 1.21AR \quad (29)$$

This equation corresponds to a maximum lift coefficient of 4.84. McCormick states that this limit can never be reached by any device attempting to increase lift by increasing circulation. The exact solution for the maximum lift coefficient for a wing of elliptic lift distribution is:

$$C_{L_{\max}} = 0.855AR \quad (30)$$

This corresponds to a $C_{L_{\max}}$ of 3.42. This limit is lower possibly due to viscous effects or the unstable vortex sheet rolling up into two discrete vortices. Equation (30) agrees more closely with experimental data for low aspect ratios and, in contrast to Equation (29), has been exceeded at increased blowing rates. From Figure 21, this investigation achieved lift coefficients closer to these theoretical limits due to increased blowing. Further results

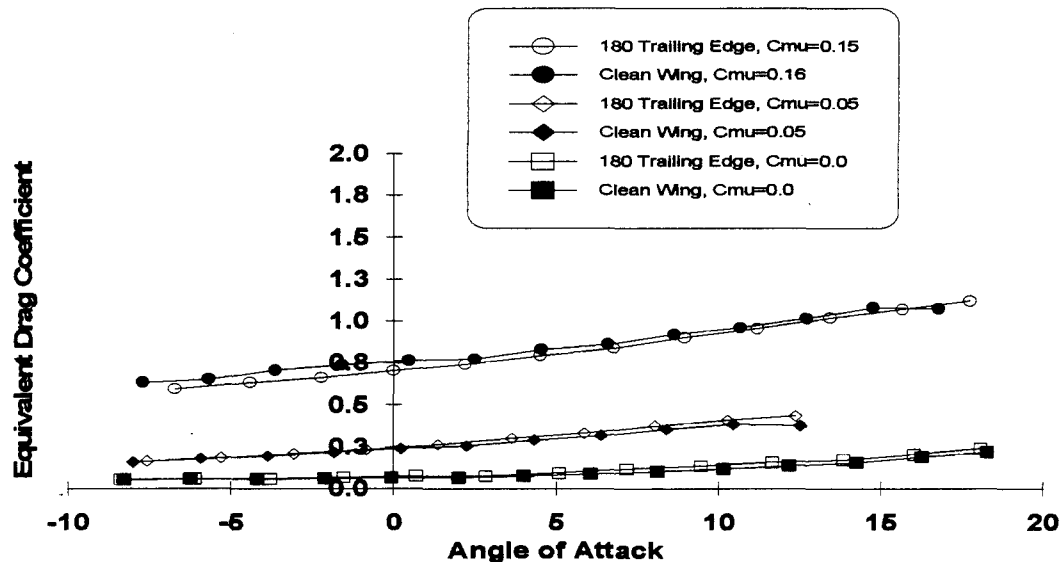


Figure 22. Comparison of Drag Performance, Clean Wing and 180 deg TE Configuration

from this investigation are compared to these limits later in this report.

In terms of the drag performance, shown in Figure 22, the difference in the C_{De} vs. α curves for the three blowing rates was on the order of 0.02 at high angles of attack. These curves reiterate the previous discussion of the drag penalty incurred when using tangential blowing.

Comparison of Modified Wing Model Aerodynamic Data

A comparison of the aerodynamic coefficients measured from the modified model configurations will be considered next. As stated in the introduction, an objective of this investigation was to determine the effects of the blowing rate as well as the effectiveness of the leading edge nose droop, splitter plate and wing tip fences on the aerodynamic data at various angles of attack.

Leading Edge Nose Droop. Figure 23 shows that the addition of the leading edge nose droop increased the stall angle of attack at $C_{\mu}=0.05$ and $C_{\mu}=0.15$. At low

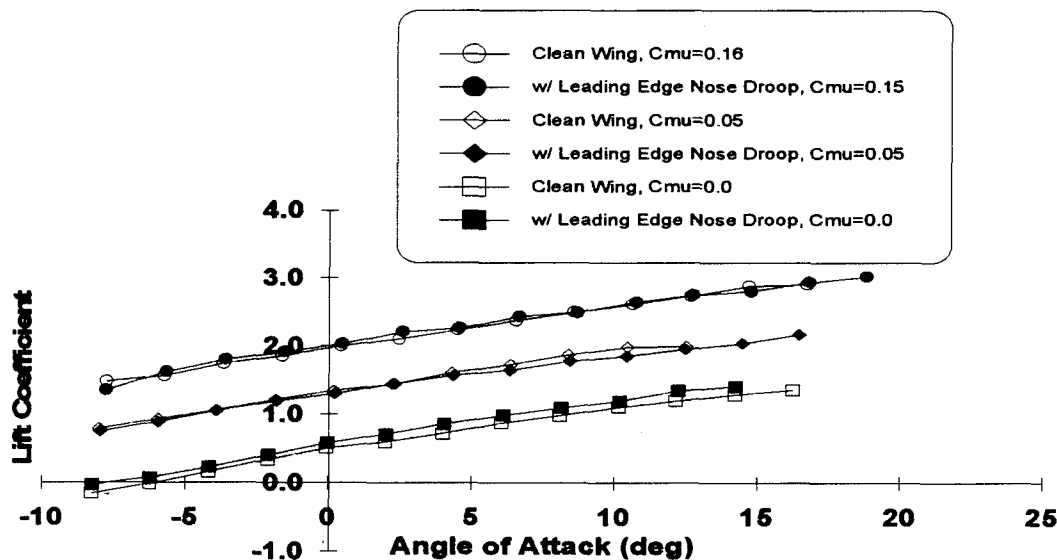


Figure 23. Effect of Leading Edge Nose Droop on Stall Angle of Attack

blowing, the clean wing configuration began to stall at 12.5 deg. The addition of the leading edge nose droop increased the stall angle to 16.5 deg. At medium blowing, the clean wing configuration began stalling at 16.8 deg. With the leading edge nose droop, the stall angle of attack was increased to 18.8 deg. The addition of the leading edge nose droop increased the camber and planform area of the wing model. As a result, the circulation was augmented and the stall angle of attack was increased.

In addition to increasing the stall angle of attack, Figure 24 shows that the leading edge nose droop decreased the pitching moment coefficient about the center of gravity as blowing was increased. At 6 deg angle of attack, the leading edge nose droop increased the lift aft of the center of gravity decreasing the positive moment coefficient. At 0 deg and -6 deg angle of attack, the leading edge nose droop increased the nose down pitching moment as blowing increased. The effect of the model incidence on the nose down pitching moment was increased with the leading edge nose droop increasing the trim

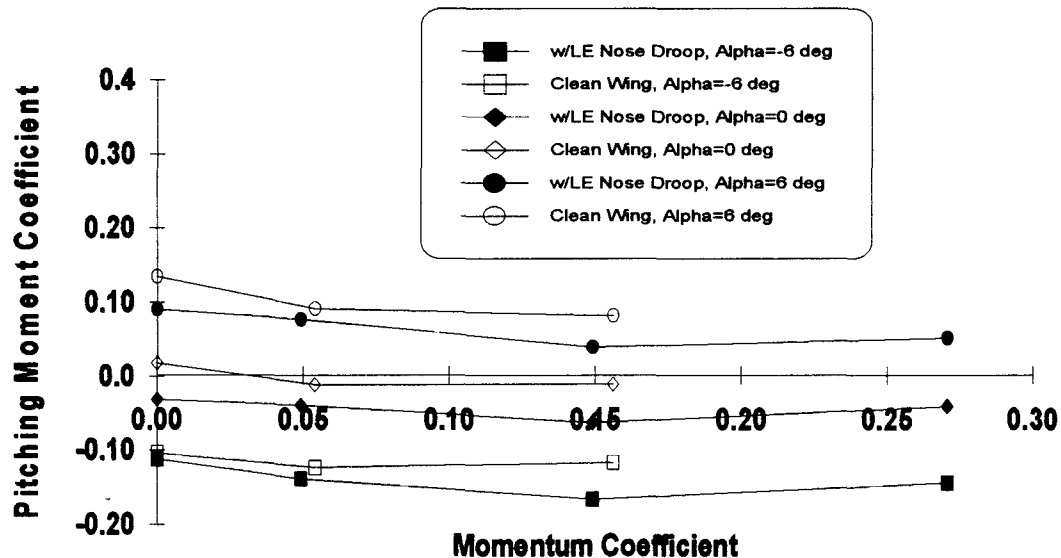


Figure 24. Effect of Leading Edge Nose Droop on Pitching Moment Coefficient

requirement at lower angles of attack. At $C_{\mu}=0.27$, the pitching moment increased. This is indicative of increased lift forward of the center of gravity.

The effect of the leading edge nose droop on the equivalent drag coefficient is shown in Figure 25. Leading edge nose droop is a means of preventing the leading edge

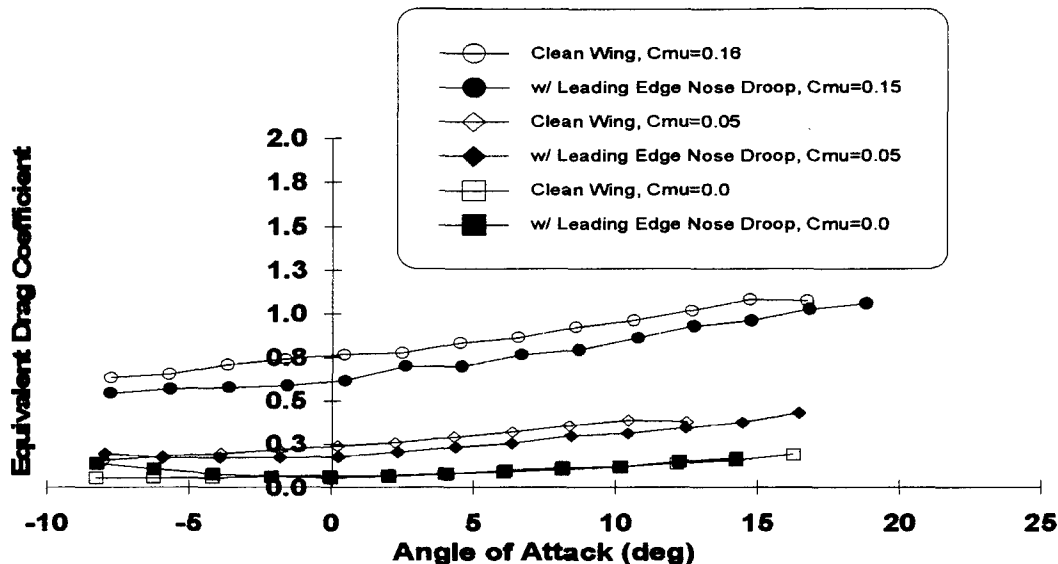


Figure 25. Effect of Leading Edge Nose Droop on Equivalent Drag

separation at high lift, hence, a decrease in the drag (24:3). The equivalent drag curve was shifted down due to the attachment of the flow at the leading edge.

Leading Edge Nose Droop and Trailing Edge Splitter Plate. The purpose of the trailing edge splitter plate was to reduce the separation effect in the form of mixing losses on the Coanda surface. The results of this test are shown in Figure 26. At low blowing rates, the increase in the lift coefficient was large, on the order of 0.8. Increasing from low blowing to higher blowing rates, the change in the lift coefficient was not as great. From $C_{\mu}=0.05$ to $C_{\mu}=0.15$, the change in the lift coefficient was on the order of 0.22. From $C_{\mu}=0.15$ to $C_{\mu}=0.27$, the increase in the lift coefficient was 0.11. This trend of

the decrease in the lift coefficient with increasing blowing rate was caused by premature

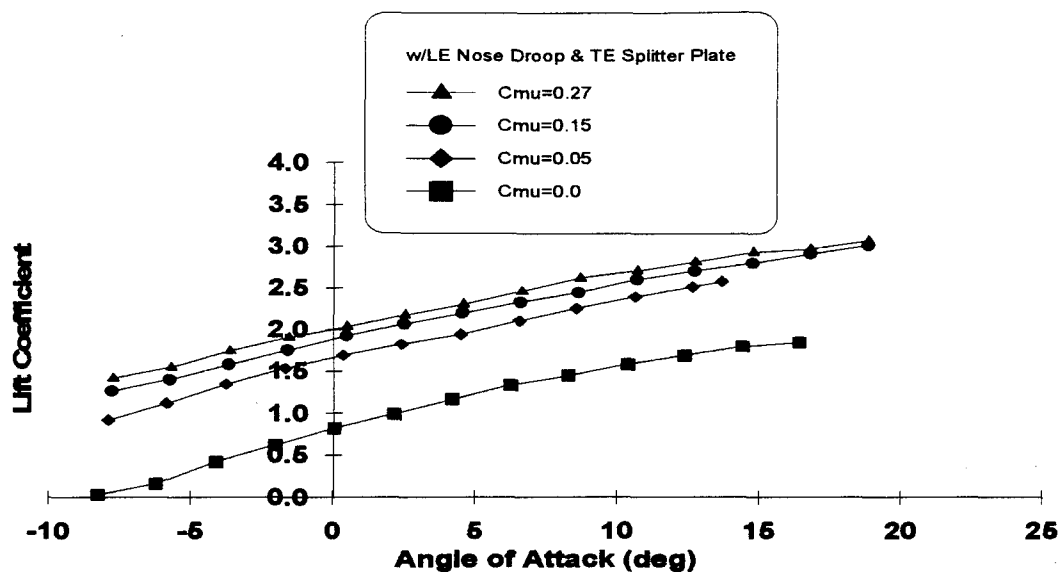


Figure 26. Effect of Blowing on Lift Coefficient, LE Nose Droop and TE Splitter Plate Configuration

separation of the air flow from the Coanda surface at the location of the splitter plate.

Figure 27 shows a comparison of the lift coefficient versus blowing rate for the LE nose droop configuration and the LE nose droop/TE splitter plate configuration. The splitter

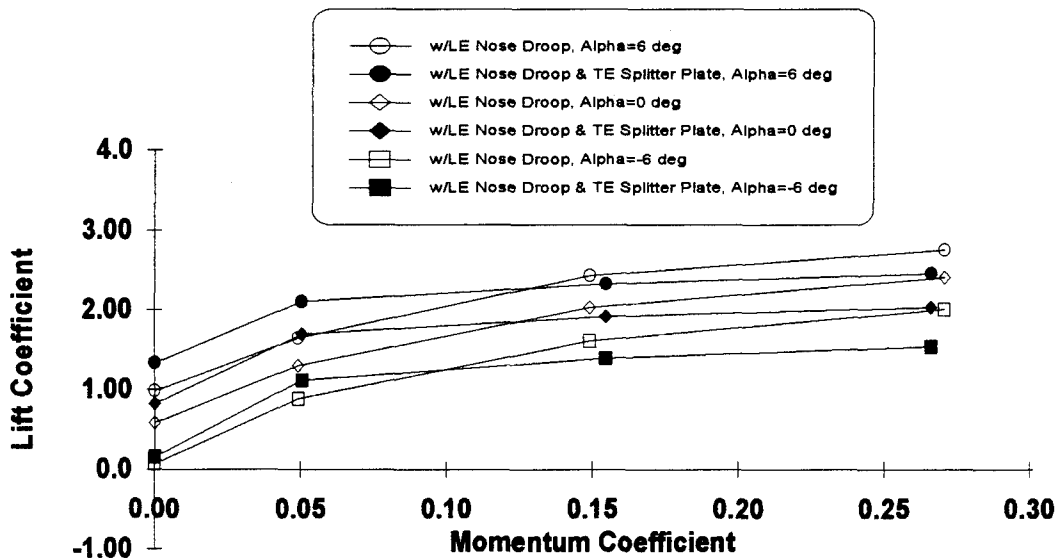


Figure 27. Effect of Trailing Edge Splitter Plate on Lift Coefficient

plate was ideally positioned to reduce separation effects at low blowing rates. For the angles of attack shown above, the slopes of the C_L vs. C_μ curve increased from 13.4 to 15.3 at $0.0 \leq C_\mu \leq 0.05$. At higher blowing rates, the velocity jet from the slot was forced to separate at the splitter plate rather than moving completely around the Coanda surface. Hence, the circulation was disrupted and the lift coefficient decreased with respect to the leading edge nose droop configuration.

In terms of the equivalent drag coefficient, Figure 28 shows that at low blowing

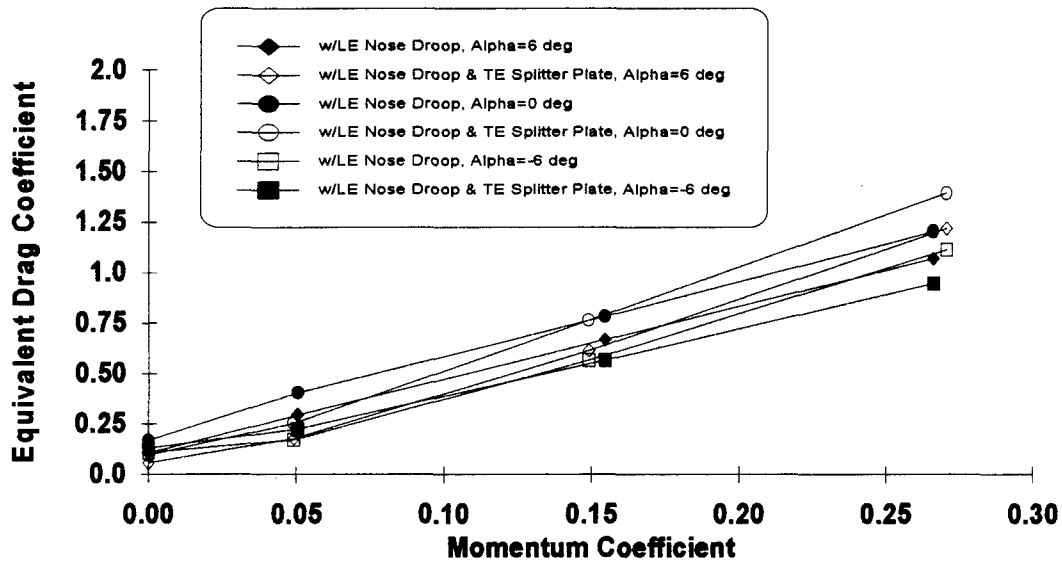


Figure 28. Effect of Trailing Edge Splitter Plate on Equivalent Drag Coefficient

rates, the equivalent drag coefficient was higher due to the increased lift. However, at $C_\mu=0.27$, the equivalent drag for the LE nose droop/TE splitter plate configuration decreased. This was the result of the decreased lift coefficient relative to the leading edge nose droop configuration caused by the splitter plate at this blowing rate.

As shown in Figure 29, the trailing edge splitter plate did not significantly affect the pitching moment about the model center of gravity. The difference in the pitching moment coefficient between the LE nose droop configuration and the LE nose droop/TE

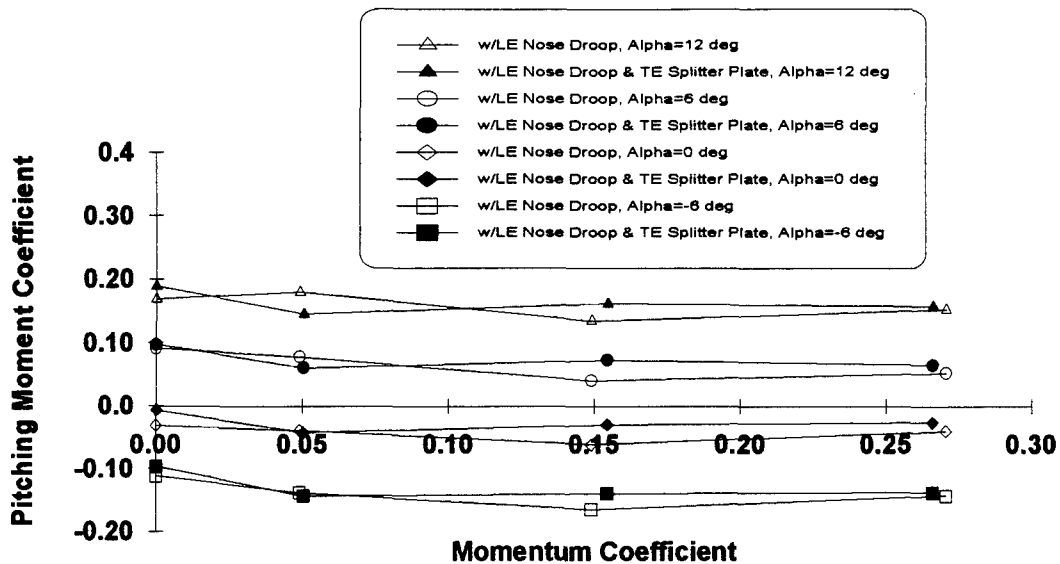


Figure 29. Effect of Trailing Edge Splitter Plate on Pitching Moment Coefficient

splitter plate configuration at a given angle of attack was due to the effect the splitter plate had on the lift.

Wing Tip Fences. The wing tip flow fences were attached to the LE Nose Droop configuration and the LE Nose Droop/TE Splitter Plate configuration. The purpose of the flow fences was to encourage attached flow on the upper surface of the model. Also, placing the flow fences at the wing tips prevented the spanwise flow of air over the surface of the model to the wing tips reducing losses.

For the leading edge nose droop configuration, shown in Figure 30, the wing tip fences were ineffective at increasing the lift capability of the model at $C_{\mu}=0.0$. However,

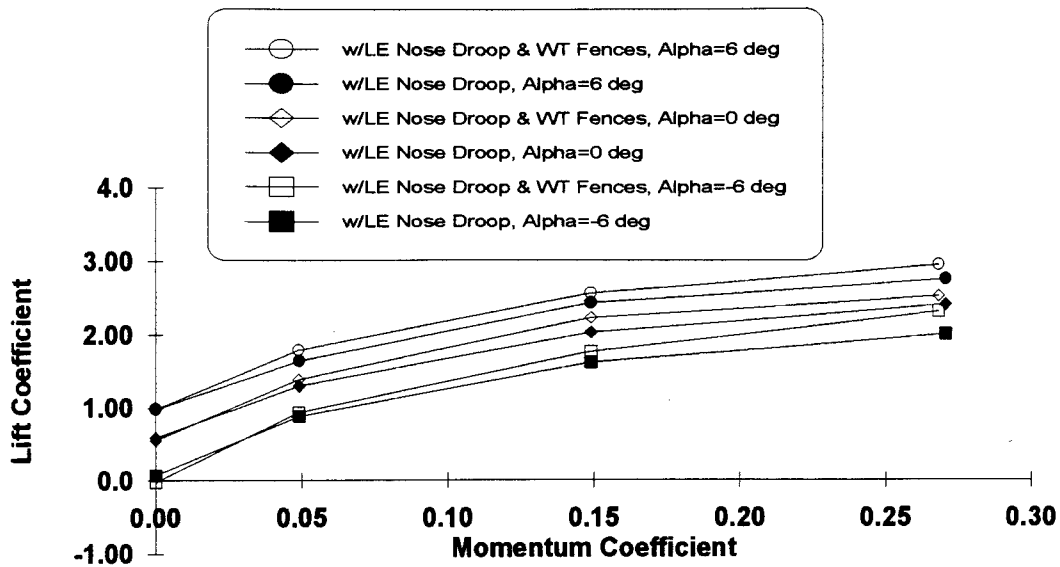


Figure 30. Effect of Wing Tip Fences on Lift Coefficient, LE Nose Droop Configuration as the blowing rate increased the lift coefficient increased. At $C_{\mu}=0.05$, at 6 deg angle of

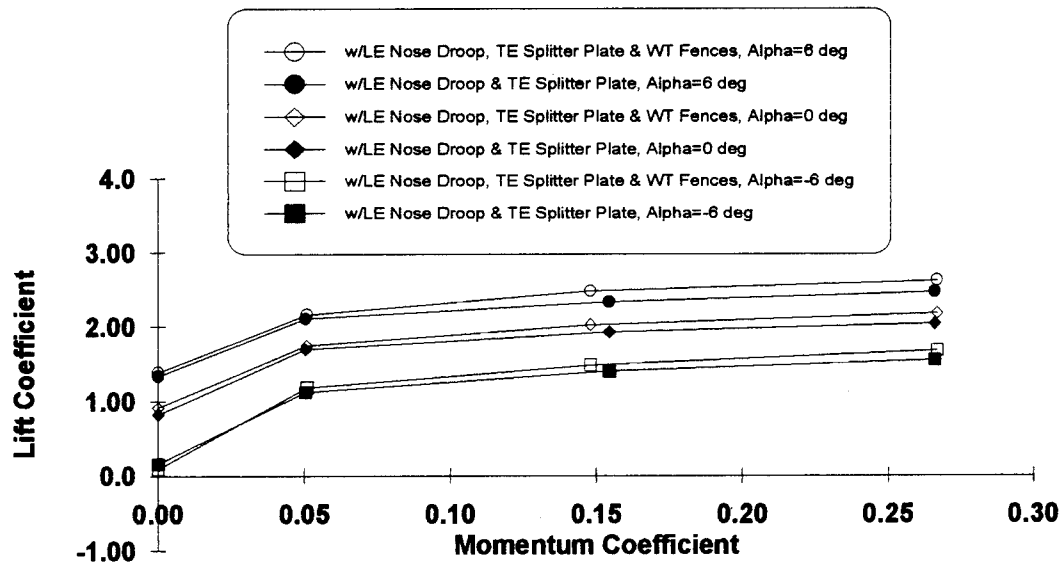


Figure 31. Effect of Wing Tip Fences on Lift Coefficient, LE Nose Droop and TE Splitter Plate Configuration

attack, the lift coefficient increased 9 percent. At $C_{\mu}=0.15$, the lift coefficient increased 10 percent at 0 and -6 deg angles of attack. At -6 deg angle of attack, the lift coefficient increased 15 percent at $C_{\mu}=0.27$. The effect of the wing tip fences on the LE nose

droop/TE splitter plate configuration is shown in Figure 31. As with the leading edge nose droop configuration, the wing tip fences had the greatest effect at the medium and higher blowing rates. At all three angles of attack shown above, the increase in the lift coefficient was on the order of 6 percent at $C_{\mu}=0.27$.

In terms of the equivalent drag, Figure 32 shows a reduction in the equivalent drag coefficient on the order of 3 percent at $C_{\mu}=0.27$. Figure 33 shows a reduction in

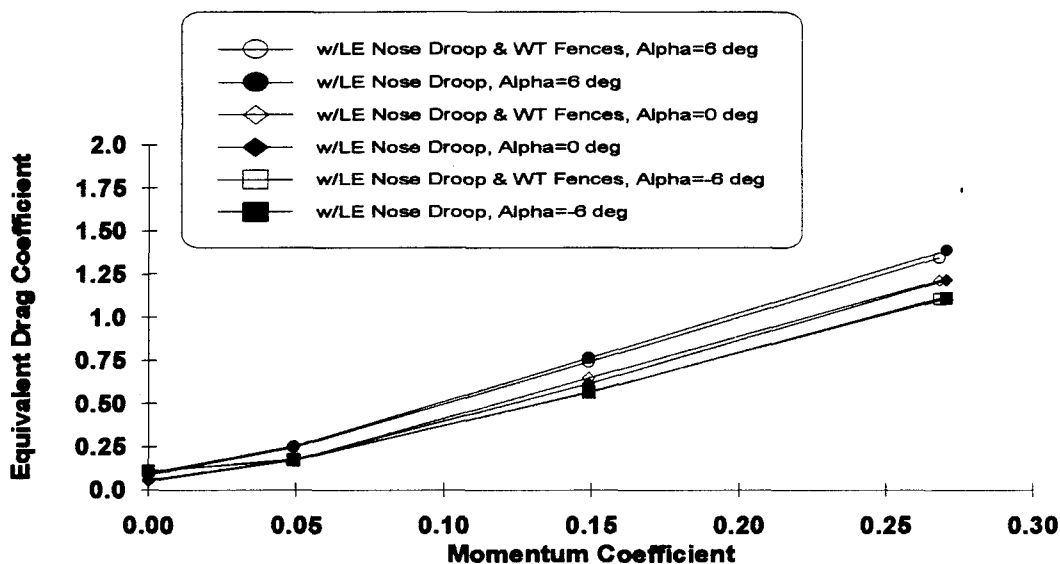


Figure 32. Effect of Wing Tip Fences on Equivalent Drag, LE Nose Droop Configuration
equivalent drag of approximately 5 percent at 0 deg angle of attack at medium blowing. The decrease in the equivalent drag for both configurations is primarily due to the decrease in induced drag caused by the flow fences.

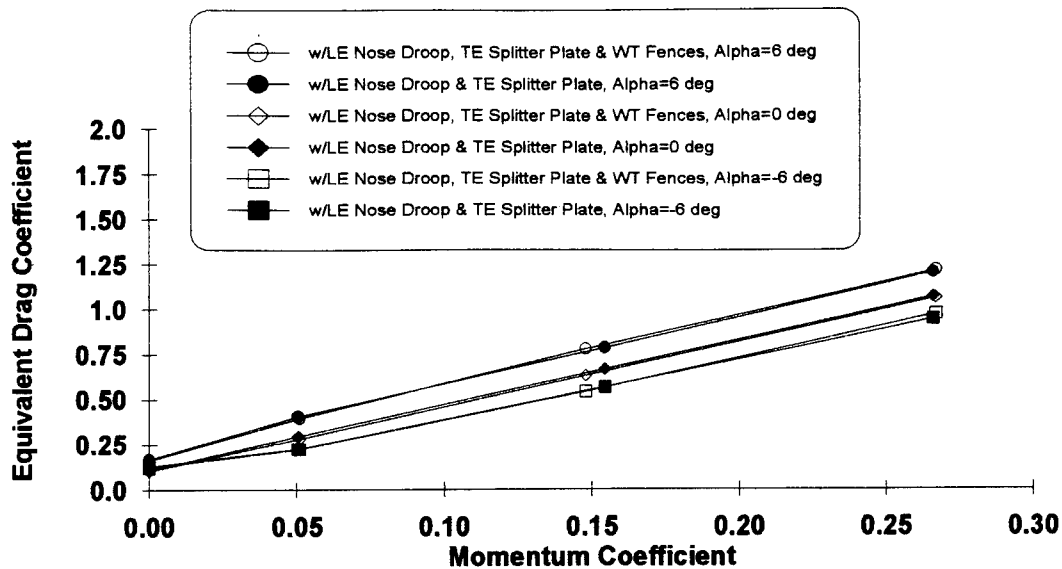


Figure 33. Effect of Wing Tip Fences on Equivalent Drag, LE Nose Droop and TE Splitter Plate Configuration

Lift Performance at Maximum Blowing

The lift performance of the model configurations at maximum blowing is compared in Figure 34. The results show that the LE nose droop with wing tip fences configuration

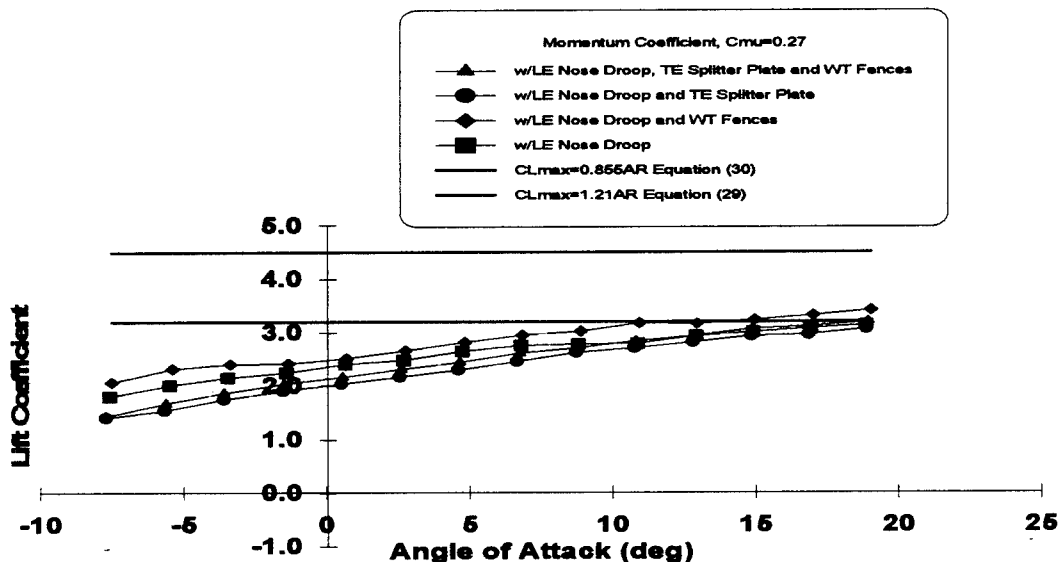


Figure 34. Lift Performance at Maximum Blowing

had the highest lift of the four configurations. At 0 deg angle of attack, the LE nose droop configuration had 4 percent less lift, the LE nose droop/TE splitter plate with wing tip fences had 16 percent less lift, and the LE nose droop/TE splitter plate configuration had 24 percent less lift.

Relative to the theoretical limits for maximum lift coefficient, the results show that the LE nose droop/TE splitter plate with wing tip fences configuration and the leading edge nose droop with wing tip fences configuration met the theoretical limit for the maximum lift coefficient provided by Equation (30) at $C_{\mu}=0.27$. These model configurations had an aspect ratio on the order of 3.7. This corresponded to a theoretical maximum lift coefficient of 3.2. The leading nose droop with wing tip configuration had a maximum lift coefficient of 3.2. The LE nose droop/TE splitter plate with wing tip configuration had a maximum lift coefficient of 3.2. Now, from McCormick (15:56), at 0 deg angle of attack with $C_{\mu}=0.25$, the value of the lift coefficient is approximately 2.0. Hence, the results from this investigation are somewhat validated. However, the theoretical limit from Equation (30) corresponds to a maximum lift coefficient of 3.2 at 0 deg angle of attack. Hence, the contribution of the increased angles of attack allowed the theoretical limits to be reached in Figure 34.

Equivalent Drag Performance at Maximum Blowing

The equivalent drag performance at maximum blowing is compared in Figure 35. The results show that at 0 deg angle of attack, the LE nose droop and LE nose droop with wing tip fences configurations had the highest drag. The LE nose droop/TE splitter plate with wing tip fences and the LE nose droop/TE splitter plate had approximately 14

percent less drag. Figure 27 shows that at $C_{\mu}=0.27$ at 0 deg angle of attack, the lift performance of the LE nose droop/TE splitter plate configuration was decreased by 18 percent relative to the performance of the leading edge nose droop configuration. Hence, this reduced drag was due to the decreased lift performance of these configurations caused by the location of the splitter plate.

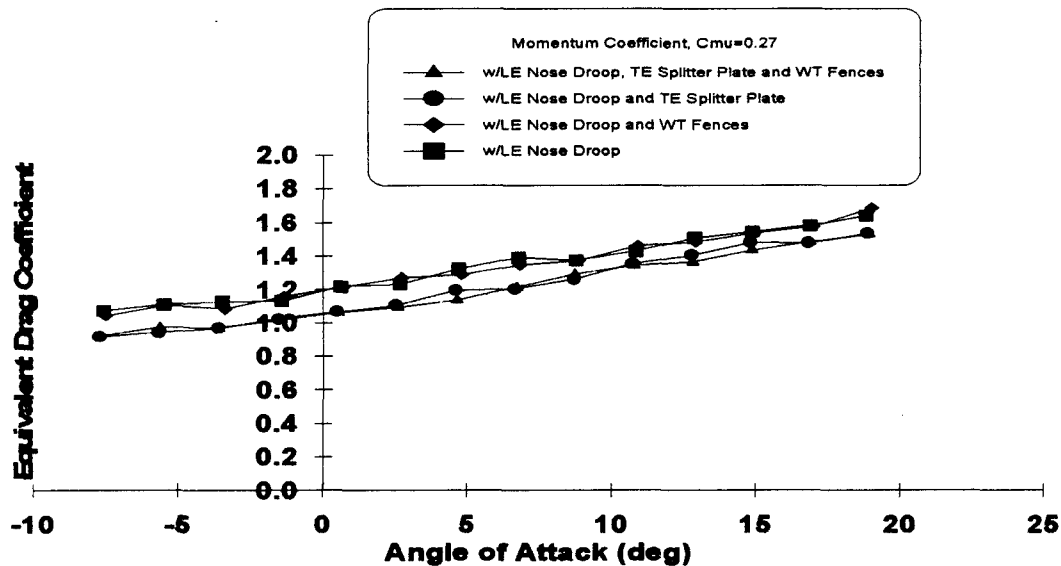


Figure 35. Equivalent Drag Performance at Maximum Blowing

Drag Polar

Typically, aerodynamic data is displayed in the form of the drag polar. The C_L vs. C_{De} curves shown in Figure 36 reflect the advantage of using tangential spanwise blowing over the Coanda trailing edge as a circulation control method to enhance the lift and drag characteristics of the wing model. The increased lift performance is especially noticeable at the medium blowing rates.

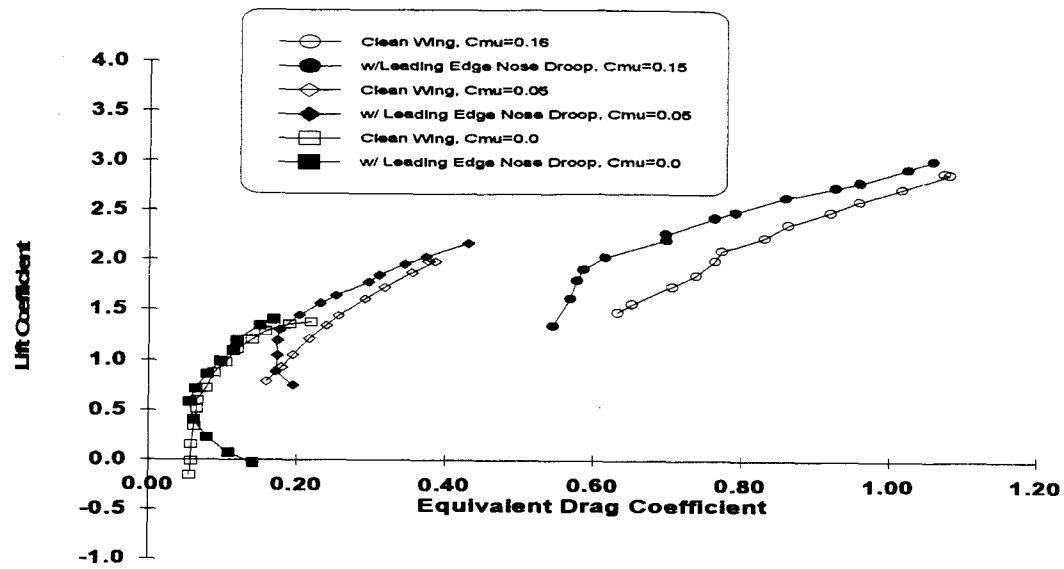


Figure 36. Drag Polar, Clean Wing and LE Nose Droop Configuration

Chapter 7. Conclusions

1. Higher blowing rates can produce higher lift coefficients. Test results show that as the blowing rate increases the rate of increase in the lift decreases indicating a limit to circulation induced lift. Agreement between the predicted lift curve slope and the experimental results validated the results of the clean wing configuration.
2. The comparison between the clean wing configuration of this investigation and the 180 deg trailing edge configuration of Tallarovic's investigation show that these tests are repeatable and validate the results. The differences in the lift coefficient can be attributed to the improvement of instrumentation in this experiment and software capability.
3. The addition of the leading edge nose droop increased the stall angle of attack by 4 deg at medium blowing and 2 deg at higher blowing. In addition, the equivalent drag was decreased approximately 17 percent at high blowing rates. The nose down pitching moment was increased, requiring increased trim requirements at 0 and negative angles of attack.
4. The test results prove that the addition of the splitter plate to the trailing edge increases lift augmentation. At the low blowing rate, the lift coefficient was increased approximately 25 percent. For higher blowing rates, the results show that the location of the splitter plate inhibits flow attachment on the Coanda surface, resulting in a considerable penalty in both the lift and drag performance. Relocation of the splitter plate is required for higher blowing rates.

5. Wing tip fences improved the lift characteristics of the model configurations approximately 15 percent at medium and high blowing rates.
6. Results show a significant increase in drag due to blowing. The equivalent drag correction ranged from 40 percent, at low blowing, to 89 percent, at high blowing, of the total drag coefficient.

Chapter 8. Recommendations

1. Further testing should be done with this model with emphasis on the splitter plate location on the Coanda surface. Several positions of the splitter plate on the trailing edge should be tested to determine the optimal location to achieve greater lift at higher blowing rates.
2. A complete pressure coefficient profile should be taken around the entire wing. It is recommended that the leading edge nose droop be instrumented to measure pressure. The location of the stagnation points as well as the possibility of a localized suction peak on the vertical surface of the trailing, as mentioned by Lacher (8:71), should be investigated.
3. Higher blowing levels should be tested in the clean wing configuration and the leading edge nose droop configuration to correlate the limits proposed by McCormick (15). The slot height should also be varied. With increased mass flow, the velocity jet becomes choked decreasing lift augmentation.
4. It is recommended that a new model be constructed with leading and trailing edge sweep and tested in the AFIT 5-ft Wind Tunnel. A fuselage mold should also be incorporated.

References

1. Englar, R. J. Low-Speed Aerodynamic Characteristics of a Small, Fixed-Trailing-Edge Circulation Control Wing Configuration Fitted to a Supercritical Airfoil. NSRDC Technical Note AL-211. Bethesda MD: Naval Ship Research and Development Center, August 1971.
2. Englar, R. J. Two-Dimensional Subsonic Wind Tunnel Investigations of a Cambered 30-Percent Thick Circulation Control Airfoil. NSRDC Technical Note AL-201. Bethesda MD: Naval Ship Research and Development Center, May 1972.
3. Englar, R. J., Trobaugh, L. A., and Hemmersly, R. A. "STOL Potential of the Circulation Control Wing for High-Performance Aircraft," Journal of Aircraft, 14: 175-181 (March 1978).
4. Englar, R. J. "Circulation Control for High Lift and Drag Generation on STOL Aircraft," Journal of Aircraft, 12: 457-463 (May 1975).
5. Kind, R. J. and Maull, D. J. "An Experimental Investigation of a Low-Speed Circulation-Controlled Aerofoil," The Aeronautical Quarterly, 19: 170-182 (May 1968).
6. Grumman Aerospace Corporation. Design of an A-6A Flight Demonstrator Aircraft Modified with a Circulation Control Wing (CCW). NSRDC Report CCW/1255-RE-01. Bethesda, MD: Naval Ship Research and Development Center, January 1978.
7. Tallarovic, J. M. An Experimental Investigation of a Finite Circulation Control Wing. MS Thesis, AFIT/GAE/ENY/92D-22. School of Engineering, Air Force Institute of Technology (AU), Wright-Patterson AFB OH, December 1992.
8. Lacher, S. J. An Experimental Study of a Sting-Mounted Circulation Control Wing. MS Thesis, AFIT/GAE/ENY/91D-4. School of Engineering, Air Force Institute of Technology (AU), Wright-Patterson AFB OH, December 1991.
9. Pelletier, M. E. An Experimental Study of a Sting-Mounted Single-Slot Circulation Control Wing. MS Thesis, AFIT/GAE/ENY/90D-18. School of Engineering, Air Force Institute of Technology (AU), Wright-Patterson AFB OH, December 1990.
10. Trainor, J. W. A Wind Tunnel Study of a Sting-Mounted Circulation Control Wing. MS Thesis, AFIT/GAE/ENY/89D-38. School of Engineering, Air Force Institute of Technology (AU), Wright-Patterson AFB OH, December 1989.

11. Harvell, J. K. An Experimental/Analytical Investigation into the Performance of a 20-Percent Thick, 8.5 Percent Cambered Circulation Controlled Airfoil. MS Thesis, AFIT/GAE/ENY/82D-13. School of Engineering, Air Force Institute of Technology (AU), Wright-Patterson AFB OH, December 1982.
12. Wood, N. J. and Nielsen, J. N. Circulation Control Airfoils Past, Present, Future. AIAA Paper 85-0204. American Institute of Aeronautics and Astronautics, January 1985.
13. Stevenson, T. A., Franke, M. E., Rhynard, W. E., and Snyder, J. R. "Wind-Tunnel Study of a Circulation-Controlled Elliptical Airfoil," Journal of Aircraft, 14: 881-886 (September 1977).
14. Rae, W. H. and Pope, A. Low Speed Wind Tunnel Testing. New York, NY: John Wiley & Sons, Inc., 1984.
15. McCormick, B. W. Aerodynamics of V/STOL Flight. Orlando, FL: Academic Press, Inc., 1967.
16. Kohlman, D. L. Introduction to V/STOL Airplanes. Ames, IA: Iowa State University Press, 1981.
17. ATMIO E Series User's Manual. National Instruments Part Number 320517C-01. March 1995 Edition. Austin, TX: National Instruments Corporation, 1995.
18. Holman, J. P. Experimental Methods for Engineers. New York, NY: McGraw-Hill, Inc., 1989.
19. Biggers, J. C. and Nielsen, J. N. Recent Progress in Circulation Control Aerodynamics. AIAA Paper 87-0001. American Institute of Aeronautics and Astronautics, January 1987.
20. Bertin, J. J. and Smith, M. L. Aerodynamics for Engineers. New York, NY: Prentice-Hall, Inc., 1989.
21. Systems Research Laboratories. AFIT 5-ft Wind Tunnel Data Acquisition System. Version 1.3, User's Manual. Wright-Patterson AFB OH, April 1990.
22. Englar, R. J. Two-Dimensional Subsonic Wind Tunnel Tests of Two 15-Percent Thick Circulation Control Airfoils. NSRDC Technical Note AL-211. Bethesda MD: Naval Ship Research and Development Center, August 1971.
23. Englar, R. J. and Williams, R. M. Test Techniques for High-Lift, Two-Dimensional Airfoils with Boundary Layer and Circulation Control for Application to Rotary Wing Aircraft. Report 4645. Bethesda MD: Naval Ship Research and Development Center, July 1975.

24. Englar, R. J. Subsonic Two-Dimensional Wind Tunnel Investigations of the High Lift Capability of Circulation Control Wing Sections. Report ASED-274. Bethesda MD: Naval Ship Research and Development Center, April 1975.

Appendix A: Reduced Force Balance Data

15 Aug 95 Aero1501
Hoses Attached Clean Wing
Patm = 29.075"Hg
Tatm = 82.7 deg F

Cmu=0.0

AOAcorr (deg)	windClcorr	windCdecorr	windCmcorr
-8.2833	-0.1550	0.0552	-0.1378
-6.2465	-0.0143	0.0570	-0.1039
-4.1883	0.1566	0.0573	-0.0642
-2.1159	0.3371	0.0613	-0.0229
-0.0650	0.5116	0.0655	0.0178
1.9955	0.5977	0.0656	0.0579
4.0049	0.7210	0.0775	0.0942
6.0605	0.8722	0.0882	0.1347
8.1107	0.9804	0.1036	0.1673
10.1553	1.1079	0.1190	0.2002
12.1726	1.2024	0.1387	0.2269
14.2495	1.2892	0.1572	0.2512
16.2655	1.3608	0.1897	0.2707
18.2707	1.3803	0.2182	0.2731

15-Aug-95 Aero1502
Hoses Attached Clean Wing
Patm = 29.12"Hg
Tatm = 87.8 deg F

Cmu=0.05

AOAcorr (deg)	windClcorr	windCdecorr	windCmcorr
-8.0010	0.7871	0.1583	-0.1553
-5.9290	0.9318	0.1791	-0.1231
-3.8727	1.0566	0.1943	-0.0852
-1.8256	1.2149	0.2158	-0.0484
0.2207	1.3465	0.2393	-0.0117
2.2540	1.4452	0.2556	0.0241
4.3264	1.6115	0.2915	0.0597
6.3792	1.7268	0.3179	0.0915
8.3957	1.8755	0.3552	0.1222
10.4643	1.9878	0.3855	0.1505
12.5208	1.9922	0.3761	0.1881

15-Sep-95 Aero1503
Hoses Attached Clean Wing
Patm = 29.13"Hg
Tatm = 87.4 deg F

Cmu=0.16

AOAcorr (deg)	windClcorr	windCdecorr	windCmcorr
-7.7344	1.4809	0.6326	-0.1458
-5.6977	1.5632	0.6519	-0.1163
-3.6543	1.7387	0.7064	-0.0798
-1.6062	1.8538	0.7388	-0.0461
0.4529	1.9991	0.7641	-0.0105
2.4845	2.1037	0.7731	0.0210
4.5329	2.2405	0.8312	0.0523
6.5836	2.3724	0.8630	0.0814
8.6106	2.5025	0.9210	0.1082
10.6502	2.6145	0.9600	0.1338
12.7026	2.7394	1.0169	0.1569
14.7449	2.8831	1.0808	0.1830
16.7688	2.9020	1.0740	0.2013

12-Sep-95 Aero1201
Hoses Attached w/ LE Nose
Droop
Patm=29.21"Hg
Tatm=76.3 deg F

Cmu = 0.0

AOAcorr (deg)	windClcorr	windCdecorr	windCmcorr
-8.2551	-0.0299	0.1404	-0.1118
-6.2324	0.0739	0.1076	-0.1121
-4.1627	0.2262	0.0782	-0.1009
-2.0991	0.4041	0.0612	-0.0702
-0.0286	0.5845	0.0553	-0.0314
2.0274	0.7112	0.0631	0.0111
4.0657	0.8592	0.0789	0.0507
6.1286	0.9863	0.0968	0.0905
8.1532	1.0967	0.1138	0.1231
10.2020	1.1963	0.1181	0.1476
12.2639	1.3481	0.1497	0.1680
14.2660	1.4080	0.1682	0.2195

12-Sep-95 Aero1202

Hoses Attached w/ LE Nose

Cmu = 0.05

Droop

Patm=29.21"Hg

Tatm=76.7 deg F

AOAcorr (deg)	windClcorr	windCdecorr	windCmcorr
-7.9648	0.7505	0.1946	-0.1454
-5.9226	0.8898	0.1712	-0.1392
-3.9185	1.0501	0.1734	-0.1148
-1.7992	1.1956	0.1730	-0.0790
0.2490	1.3031	0.1763	-0.0395
2.3409	1.4491	0.2029	-0.0017
4.3784	1.5698	0.2312	0.0345
6.3618	1.6464	0.2522	0.0769
8.4533	1.7798	0.2965	0.1084
10.4401	1.8499	0.3108	0.1434
12.4895	1.9583	0.3450	0.1792
14.4830	2.0404	0.3733	0.2095
16.4725	2.1725	0.4303	0.2224

12-Sep-95 Aero1203

Hoses Attached w/ LE Nose

Cmu = 0.15

Droop

Patm=29.193"Hg

Tatm=79.1 deg F

AOAcorr (deg)	windClcorr	windCdecorr	windCmcorr
-7.7553	1.3485	0.5448	-0.1793
-5.6455	1.6208	0.5685	-0.1654
-3.5923	1.8000	0.5773	-0.1351
-1.5353	1.9113	0.5863	-0.0963
0.4934	2.0324	0.6151	-0.0624
2.6103	2.2095	0.6978	-0.0260
4.5947	2.2680	0.6975	0.0080
6.6857	2.4369	0.7637	0.0396
8.7247	2.4967	0.7917	0.0795
10.7979	2.6474	0.8597	0.1033
12.7675	2.7541	0.9270	0.1339
14.7944	2.8051	0.9600	0.1622
16.8424	2.9401	1.0249	0.1893
18.8492	3.0254	1.0591	0.2109

12-Sep-95

Aero1205

Hoses Attached w/LE Nose

Cmu = 0.27

Droop

Patm=29.181"Hg

Tatm=80.9 deg F

AOAcorr (deg)	windClcorr	windCdecorr	windCmcorr
-7.5885	1.8098	1.0751	-0.1737
-5.5008	2.0112	1.1126	-0.1438
-3.4680	2.1572	1.1299	-0.1110
-1.4192	2.2563	1.1335	-0.0768
0.6359	2.4076	1.2176	-0.0408
2.6723	2.4870	1.2336	-0.0097
4.7231	2.6493	1.3245	0.0230
6.7836	2.7549	1.3899	0.0517
8.7745	2.7778	1.3727	0.0861
10.8527	2.7898	1.4284	0.1273
12.8987	2.9402	1.5078	0.1520
14.8989	3.0127	1.5444	0.1743
16.9118	3.0872	1.5810	0.2000
18.8501	3.1382	1.6393	0.2261

13-Sep-95

Aero1301

Hoses Attached w/WT Fences

Cmu = 0.0

and LE Nose Droop

Patm=29.101"Hg

Tatm=78.8 deg F

AOAcorr (deg)	windClcorr	windCdecorr	windCmcorr
-8.2952	-0.1464	0.1504	-0.1016
-6.2409	-0.0215	0.1086	-0.1066
-4.2202	0.1490	0.0743	-0.0963
-2.1037	0.3653	0.0577	-0.0629
-0.0247	0.5515	0.0506	-0.0218
2.0207	0.7032	0.0559	0.0207
4.0852	0.8539	0.0669	0.0628
6.1253	0.9822	0.0874	0.0994
8.1689	1.1158	0.1017	0.1368
10.2117	1.2003	0.1071	0.1711
12.2505	1.2832	0.1193	0.2065
14.2679	1.3996	0.1422	0.2378

13-Sep-95 Aero1302
Hoses Attached w/WT Fences
and LE Nose Droop
Patm=29.098"Hg
Tatm=80.3 deg F

Cmu = 0.05

AOAcorr (deg)	windClcorr	windCdecorr	windCmcorr
-7.9732	0.7492	0.1889	-0.1433
-5.9150	0.9410	0.1771	-0.1406
-3.8459	1.1082	0.1683	-0.1145
-1.7813	1.2580	0.1669	-0.0780
0.2861	1.3972	0.1708	-0.0383
2.3067	1.5193	0.1898	-0.0003
4.3703	1.6755	0.2274	0.0366
6.4173	1.7979	0.2474	0.0748
8.4994	1.9056	0.2729	0.1125
10.5257	2.0073	0.3004	0.1518
12.5242	2.0782	0.3304	0.1897
14.5085	2.0908	0.3375	0.2279

13-Sep-95 Aero1304
Hoses Attached w/WT Fences
and LE Nose Droop
Patm=29.099"Hg
Tatm=81.4 deg F

Cmu = 0.15

AOAcorr (deg)	windClcorr	windCdecorr	windCmcorr
-7.6672	1.5682	0.5574	-0.1937
-5.6065	1.7728	0.5625	-0.1724
-3.5548	1.9039	0.5523	-0.1389
-1.4791	2.0763	0.5938	-0.1032
0.5760	2.2354	0.6480	-0.0671
2.6275	2.3601	0.6707	-0.0314
4.6760	2.4947	0.7222	0.0069
6.7031	2.5677	0.7401	0.0442
8.7357	2.6892	0.8154	0.0835
10.7733	2.7454	0.8255	0.1185
12.8204	2.8658	0.8770	0.1440
14.8950	3.0010	0.9532	0.1742
16.8903	3.0557	0.9702	0.2015
18.9323	3.1728	1.0648	0.2296

13-Sep-95 Aero1305
Hoses Attached w/WT Fences
and LE Nose Droop
Patm=29.089"Hg
Tatm=84.5 deg F

Cmu = 0.27

AOAcorr (deg)	windClcorr	windCdecorr	windCmcorr
-7.5164	2.0690	1.0452	-0.1922
-5.3929	2.3192	1.1102	-0.1648
-3.3745	2.4058	1.0847	-0.1288
-1.3549	2.4203	1.1578	-0.0749
0.6822	2.5222	1.2159	-0.0336
2.7405	2.6650	1.2702	0.0005
4.8159	2.8145	1.2889	0.0232
6.8466	2.9432	1.3471	0.0584
8.8746	3.0247	1.3737	0.0893
10.9264	3.1766	1.4603	0.1167
12.9405	3.1623	1.4836	0.1610
14.9624	3.2415	1.5375	0.1881
17.0114	3.3177	1.5754	0.2131
19.0419	3.4238	1.6847	0.2320

28-Aug-95 Aero2802
Hoses Attached w/LE Nose
Droop and TE Splitter Plate
Patm=29.184"Hg
Tatm=83.6 deg F

Cmu = 0.0

AOAcorr (deg)	windClcorr	windCdecorr	windCmcorr
-8.2698	0.0317	0.1510	-0.0933
-6.2204	0.1592	0.1292	-0.0971
-4.1064	0.4192	0.1094	-0.0782
-2.0151	0.6217	0.1019	-0.0449
0.0571	0.8206	0.1057	-0.0071
2.1677	0.9916	0.1170	0.0318
4.1914	1.1662	0.1413	0.0625
6.2667	1.3363	0.1677	0.0968
8.2986	1.4480	0.1888	0.1288
10.3920	1.5819	0.2210	0.1576
12.3907	1.6884	0.2443	0.1882
14.4438	1.8015	0.2809	0.2189
16.4373	1.8467	0.3027	0.2415

28-Aug-95 Aero2804

Hoses Attached w/LE Nose

Cmu = 0.05

Droop and TE Splitter Plate

Patm=29.184"Hg

Tatm=83.6 deg F

AOAcorr (deg)	windClcorr	windCdecorr	windCmcorr
-7.9082	0.9176	0.2183	-0.1509
-5.8425	1.1183	0.2239	-0.1441
-3.7589	1.3466	0.2418	-0.1174
-1.6753	1.5408	0.2662	-0.0815
0.3706	1.6942	0.2962	-0.0432
2.4231	1.8237	0.3239	0.0063
4.5046	1.9416	0.3638	0.0335
6.5805	2.1060	0.4062	0.0598
8.5780	2.2518	0.4566	0.0891
10.6487	2.3932	0.5010	0.1184
12.6681	2.5126	0.5425	0.1447
13.7044	2.5805	0.5762	0.1544

29-Aug-95 Aero2902

Hoses Attached w/LE Nose

Cmu = 0.15

Droop and TE Splitter Plate

Patm=29.183"Hg

Tatm=84.5 deg F

AOAcorr (deg)	windClcorr	windCdecorr	windCmcorr
-7.7772	1.2625	0.5357	-0.1524
-5.7433	1.3980	0.5666	-0.1401
-3.6614	1.5806	0.5968	-0.1038
-1.5928	1.7567	0.6140	-0.0675
0.4846	1.9243	0.6679	-0.0307
2.5102	2.0616	0.7042	0.0049
4.5551	2.1949	0.7395	0.0386
6.6013	2.3294	0.7836	0.0721
8.6549	2.4447	0.8368	0.1015
10.7028	2.5985	0.9155	0.1305
12.7490	2.7051	0.9483	0.1608
14.7831	2.7998	0.9892	0.1856
16.8232	2.9104	1.0494	0.2090
18.8786	3.0098	1.0924	0.2331

29-Aug-95 Aero2903

Hoses Attached w/LE Nose

Cmu = 0.27

Droop and TE Splitter Plate

Patm=29.179"Hg

Tatm=88.3 deg F

AOAcorr (deg)	windClcorr	windCdecorr	windCmcorr
-7.7268	1.4174	0.9183	-0.1581
-5.6749	1.5467	0.9433	-0.1384
-3.6098	1.7452	0.9688	-0.1042
-1.5367	1.9074	1.0236	-0.0659
0.5006	2.0321	1.0686	-0.0271
2.5409	2.1715	1.1061	0.0041
4.5991	2.3016	1.1941	0.0406
6.6538	2.4604	1.2027	0.0645
8.7198	2.6199	1.2607	0.0961
10.7362	2.7115	1.3542	0.1241
12.7879	2.8158	1.4047	0.1567
14.8336	2.9333	1.4807	0.1799
16.8418	2.9667	1.4768	0.2062
18.8829	3.0642	1.5348	0.2322

31-Aug-95 Aero3104

Hoses Attached w/WT Fences, LE

Cmu = 0.0

Nose Droop and TE Splitter Plate

Patm=29.02"Hg

Tatm=90.7 deg F

AOAcorr (deg)	windClcorr	windCdecorr	windCmcorr
-8.2566	-0.0630	0.1559	-0.1015
-6.2169	0.0889	0.1200	-0.1016
-4.1222	0.3646	0.0913	-0.0932
-2.0017	0.6513	0.0921	-0.0627
0.1115	0.9136	0.1008	-0.0159
2.1481	1.0775	0.1119	0.0251
4.2078	1.2258	0.1329	0.0640
6.2690	1.3878	0.1600	0.1000
8.3517	1.5718	0.1948	0.1278
10.3702	1.6457	0.2118	0.1676
12.4109	1.7300	0.2318	0.2023
14.4367	1.8171	0.2566	0.2374

06-Sep-95 Aero0601
Hoses Attached w/WT Fences, LE
Nose Droop and TE Splitter Plate
Patm=29.298"Hg
Tatm=81.3 deg F

Cmu = 0.05

AOAcorr (deg)	windClcorr	windCdecorr	windCmcorr
-7.9014	0.9306	0.2261	-0.1510
-5.8118	1.1801	0.2234	-0.1465
-3.7298	1.3943	0.2366	-0.1176
-1.6652	1.5838	0.2497	-0.0826
0.4047	1.7415	0.2806	-0.0438
2.4501	1.8976	0.3187	-0.0065
4.5028	2.0368	0.3609	0.0305
6.5477	2.1592	0.3959	0.0651
8.6062	2.2834	0.4380	0.0998
10.6282	2.3809	0.4739	0.1327
12.5943	2.4661	0.5118	0.1656

31-Aug-95 Aero3102
Hoses Attached w/WT Fences, LE
Nose Droop and TE Splitter Plate
Patm=29.05"Hg
Tatm=87.6 deg F

Cmu = 0.15

AOAcorr (deg)	windClcorr	windCdecorr	windCmcorr
-7.8049	1.2178	0.5105	-0.1579
-5.7010	1.4835	0.5419	-0.1426
-3.6226	1.6905	0.5670	-0.1103
-1.5564	1.8655	0.5772	-0.0739
0.4973	2.0237	0.6307	-0.0370
2.5609	2.1806	0.6876	0.0006
4.6003	2.3029	0.7079	0.0359
6.6739	2.4723	0.7767	0.0705
8.7172	2.5988	0.8260	0.1024
10.7804	2.7380	0.8787	0.1346
12.8049	2.8706	0.9398	0.1630
14.8410	2.9649	0.9945	0.1912
16.9088	3.0463	1.0392	0.2180

31-Aug-95 Aero3103
Hoses Attached w/WT Fences, LE
Nose Droop and TE Splitter Plate
Patm=29.037"Hg
Tatm=90.2 deg F

Cmu = 0.27

AOAcorr (deg)	windClcorr	windCdecorr	windCmcorr
-7.7312	1.4406	0.9205	-0.1664
-5.6263	1.6766	0.9739	-0.1443
-3.6007	1.8699	0.9699	-0.1108
-1.4900	2.0411	1.0185	-0.0717
0.5449	2.1733	1.0633	-0.0340
2.6058	2.3091	1.0957	0.0032
4.6508	2.4403	1.1358	0.0381
6.7374	2.6144	1.2150	0.0738
8.7498	2.7143	1.2905	0.1069
10.7941	2.8357	1.3436	0.1364
12.8399	2.9352	1.3634	0.1650
14.8872	3.0633	1.4360	0.1957
16.8911	3.1216	1.4832	0.2196
18.9348	3.2088	1.5308	0.2440

Hysteresis Test

28-Aug-95 Aero2801
Hoses Attached w/LE Nose Droop
and TE Splitter Plate

$C_{mu} = 0.0$

Patm=29.19"Hg

Tatm=79 deg F

AOAcorr (deg)	windClcorr
-8.2813	0.0025
-6.2782	0.1293
-4.2585	0.3866
-2.2408	0.5865
-0.2408	0.7837
1.8077	0.9538
3.7680	1.1283
5.7816	1.2995
7.7729	1.4136
9.8177	1.5506
11.7777	1.6615
13.7897	1.7559
15.7668	1.8314
13.7921	1.7515
11.7859	1.6563
9.7741	1.5576
7.7705	1.4399
5.7695	1.2774
3.7617	1.1481
1.7583	0.9816
-0.2387	0.8008
-2.2334	0.6096
-4.2404	0.3637
-6.2769	0.1163
-8.2414	0.0231

Repeatability Test

31-Aug-95 Aero3101
Hoses Attached w/LE Nose Droop
and TE Splitter Plate
Patm=29.055"Hg
Tatm=85.7 deg F

Cmu = 0.0

AOAcorr (deg)	windClcorr	windCdecorr	windCmcorr
-8.23204	0.02564	0.14153	-0.10657
-6.19744	0.20905	0.11268	-0.10155
-4.09334	0.47242	0.09168	-0.08504
-1.97791	0.70991	0.08902	-0.05258
0.09189	0.91000	0.09569	-0.01380
2.19099	1.07442	0.11199	0.02643
4.21974	1.23525	0.13747	0.06447
6.29922	1.37385	0.16272	0.10228
8.34955	1.47851	0.18258	0.13565
10.37097	1.59537	0.20691	0.17022
12.37919	1.68819	0.23247	0.19905
14.42917	1.80201	0.25910	0.23354
16.46498	1.87971	0.28727	0.25999

Repeatability Check of Aero3101:

6-Sep-95 Aero0602
Hoses Attached w/LE Nose Droop
and TE Splitter Plate
Patm=29.292"Hg
Tatm=81.3 deg F

Cmu = 0.0

AOAcorr (deg)	windClcorr	windCdecorr	windCmcorr
-8.22632	0.02257	0.14910	-0.10495
-1.98798	0.68798	0.09705	-0.05268
4.19898	1.19765	0.14633	0.06149
10.33177	1.55327	0.21380	0.16455

Appendix B: LabVIEW® Front Panel and Wiring Diagram

Front Panel

raw force filename
rawf1205

save data? (.avg)
☐ OFF

raw voltage filename
rawv1205

save data? (.avg)
☐ OFF

thrust/tare?
☐ OFF

raw force path
c:\chelacqdata

append?
☐ OFF

raw voltage path
c:\chelacqdata

append?
☐ OFF

thrust is "on"
tare is "off"

save data must
be on to take
thrust or tares

The correction buttons to the right should be all be on when taking data. "Equivalent" should always be on to get drag without the tunnel and 3-D corrections

aero data file name
aero1201

save data? (.avg)
☐ OFF

aero data path
c:\chelacqdata

append?
☐ OFF

zero save file name
zero1205

save zero? (.avg)
☐ OFF

subtract zero voltage
☐ OFF

thrust/tare file name
tare1202

save data? (.avg)
☐ OFF

zero save path
c:\chelzeropt

Subtract the zero
voltage after the
zero point is taken.

thrust/tare path
c:\chel\tare

append?
☐ OFF

scans
300

rate
2400.00

AOAu-w(deg)
0.003

Bouyancy
☐ OFF

Induced
☐ OFF

Base Pressure
☐ OFF

Equivalent
☐ OFF

dev1 chan list
0 0.7

chan limits
high 10.00
low -10.00

dev2 chan list
0 0

chan limits
high 0.02
low -0.02

dev3 chan list
0 0.2

chan limits
high 10.00
low -10.00

Patm (Hg)	TunQ (psi)	Qcalc (psi)	Qinf (psi)	Pbase (psi)	Ptest (psi)	Ptest2 (psi)	Ptotrp (psi)	P1mass (psi)	P2mass (psi)
29.181	0.00184	0.00184	0.00184	0.00615	14.2871	14.2871	0.328	0.093	0.115
Tatm (F)	Tuntemp (R)	Tmass (R)	TFrp (R)	TBlp (R)	TBrp (R)	TFlp (R)	Ptotlp (psi)	Mass flow (slug/sec)	
80.90	542.38	526.86	544.63	541.56	408.07	385.61	0.189	NaN	
Chord (ft)	N1 (volts)	N2 (volts)	Y1 (volts)	Y2 (volts)	RM (volts)	AX (volts)	Excitation (volts)	Jet Velocity (fps)	
0.5151	-0.0189	-0.0200	-0.0106	0.0683	-0.0870	0.1696	6.0206	183.66	
Wing Area (ft^2)	Mach #	Vinf (mph)	Mu (lb-s/ft^2)	Reynolds Number		Cmu			
0.9953	0.0136	10.56	3.8696E-7	45582.35		NaN			
Model Volume (ft^3)	Xcg (ft)	Forces (minus zero point)			Forces (without tares)			Normal Force (lbs)	
0.0551	-0.01425	0	-0.503707	N1	0	-1.075329	Normal force	-1.08605	
Tunnel Area (ft^2)	Zcg (ft)		-0.571622	N2		0.738951	Yaw force	Axial Force (lbs)	
19.63495	0.04119		-0.097433	Y1		2.449372	Axial force	2.40724	
CI (thrust)	wb	sb	0.836384	Y2		0.005943	Pitch moment	Pitch Moment (lbs-ft)	
-3.5642	0.0997	0.0006	-0.073410	RM		-0.066145	Yaw moment	0.00405	
			2.449372	AX		-0.073410	Roll moment		

bodyCDe
6.50197

bodyCL
-2.9334

WindCDe
6.5018

WindCL
-2.93386

WindCm
0.4600

AOAu-w(deg)
0.003

Cdinduced
0.00000

Cdequivalent
0.00000

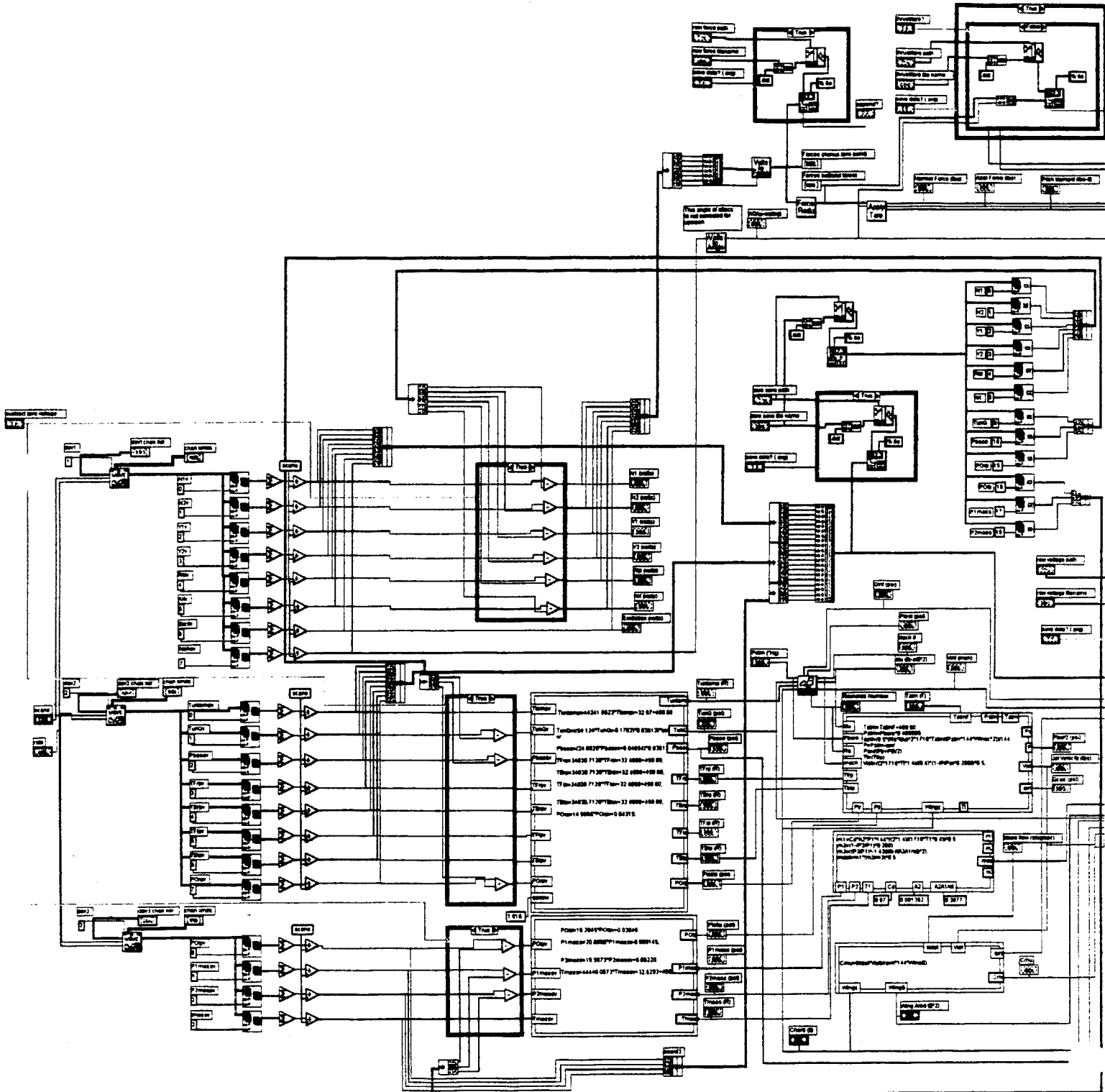
CdPbase
0.00000

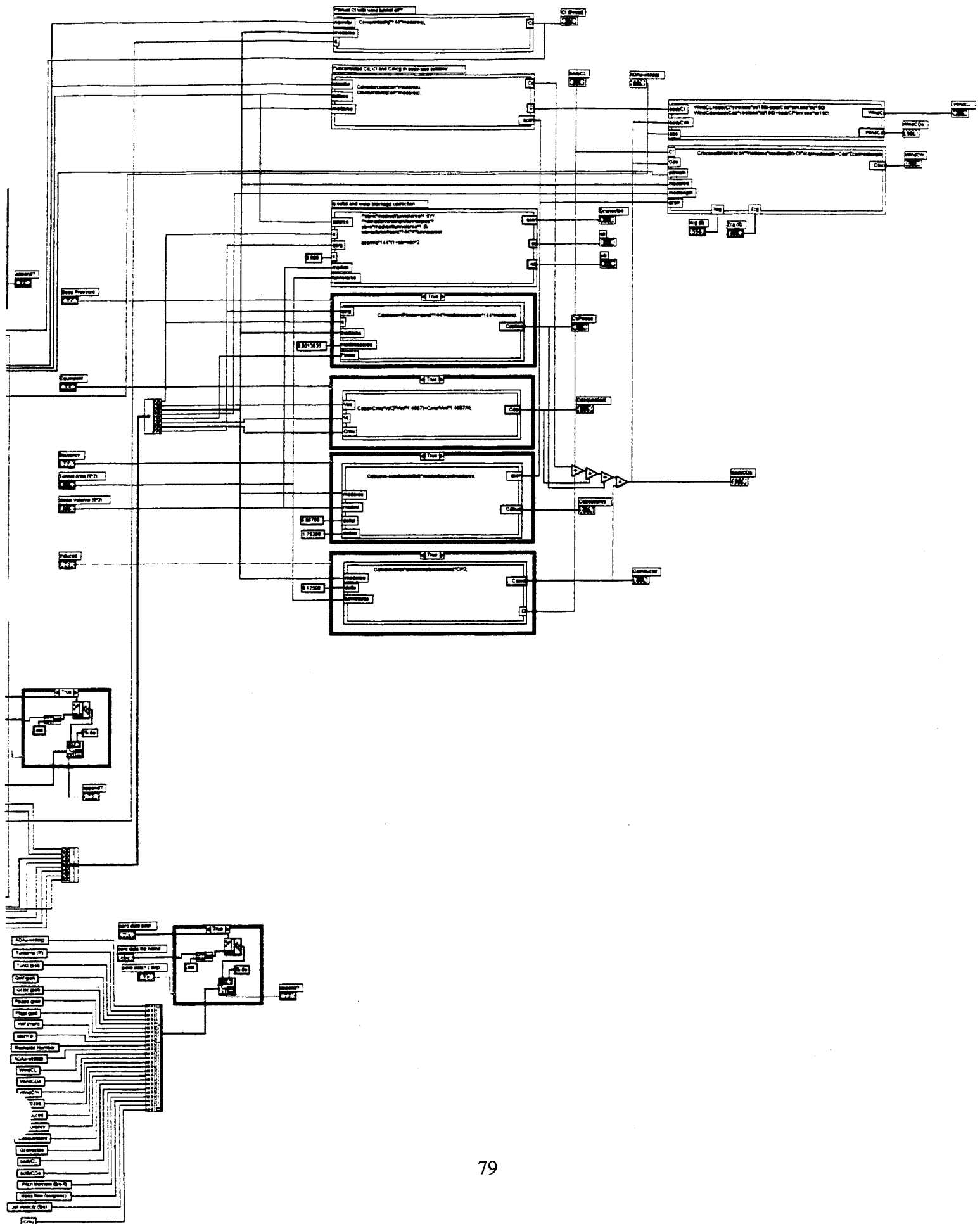
Qcorrected
0.37198

Cdbouyancy
0.00000

These values of lift and drag coefficient are in the body-axis system.

These values of lift, drag and pitching moment are in the wind-axis system





Appendix C: Data Uncertainty

Data Acquisition System

The ATMIO-16(L) data acquisition card acquired all force balance and wind tunnel pressure and temperature voltages to six significant figures. The multifunction I/O board had a precision of 4.88 mV for an input range of ± 10.00 V. This results in an accuracy of ± 2.44 mV.

Atmospheric Data Measurements

Atmospheric pressure was recorded from a mercury barometer accurate to 3.377 N/m² (± 0.001 in Hg) and corrected for temperature and error. Atmospheric temperature was recorded from a mercury thermometer accurate to ± 0.5 deg F.

Force Balance and Wind Tunnel Measurements

Force voltages were recorded from the Able Corporation Mark V 1.27 cm (0.5 in) six-component balance. The balance was accurate to ± 1 percent of full scale in each direction. The maximum pressure of the Statham pressure transducer used to record tunnel dynamic pressure was 103.4 kPa (15 psig) at 11 VDC. The accuracy of the pressure transducer was ± 1034 Pa (± 0.15 psid). Tunnel temperature was recorded using a Type T copper thermocouple accurate to 0.75 percent of full scale.

Venturi Mass Flow Measurements

Venturi mass flow and model plenum pressures were recorded from pressure transducers accurate to ± 3 mV/psi. Venturi mass flow temperature was recorded using a Type K Nickel-Chromium thermocouple accurate to ± 0.75 percent of full

scale. Plenum temperatures were recorded using a Type J Iron thermocouple accurate to ± 0.75 percent of full scale.

Center of Gravity Location

The location of the center of gravity of the wing model was determined from the data acquisition system when tare slopes were computed. It was determined that the weights of the leading edge nose droop and trailing edge splitter plate were too small to affect the location of the center of gravity. Hence, when these modifications were made to the wing model, the center of gravity location was not altered for the data reduction of these configurations.

Overall Accuracy

An uncertainty analysis of this investigation consisted of acquiring several measurements of the aerodynamic data at a single data point over time. The overall accuracy of this investigation was to within 4.3 percent for the maximum deviation.

Vita

Second Lieutenant Lorenzo C. Bradley III [REDACTED]

[REDACTED] He graduated from North Hardin High School in Radcliff, Kentucky in 1990 and entered undergraduate studies at the United States Air Force Academy in Colorado Springs, Colorado. He graduated with a Bachelor of Science degree in Aeronautical Engineering and received his commission on June 1, 1994. He entered the School of Engineering, Air Force Institute of Technology on June 27, 1994.

[REDACTED] [REDACTED]
[REDACTED] [REDACTED]

REPORT DOCUMENTATION PAGE			Form Approved OMB No. 0704-0188	
Public reporting burden for this collection of information is estimated to average 1 hour per response, including the time for reviewing instructions, searching existing data sources, gathering and maintaining the data needed, and completing and reviewing the collection of information. Send comments regarding this burden estimate or any other aspect of this collection of information, including suggestions for reducing this burden, to Washington Headquarters Services, Directorate for Information Operations and Reports, 1215 Jefferson Davis Highway, Suite 1204, Arlington, VA 22202-4302, and to the Office of Management and Budget, Paperwork Reduction Project (0704-0188), Washington, DC 20503.				
1. AGENCY USE ONLY (Leave blank)	2. REPORT DATE December 1995	3. REPORT TYPE AND DATES COVERED Master's Thesis		
4. TITLE AND SUBTITLE AN EXPERIMENTAL INVESTIGATION OF A STING-MOUNTED FINITE CIRCULATION CONTROL WING			5. FUNDING NUMBERS	
6. AUTHOR(S) Lorenzo C. Bradley III, Second Lieutenant, USAF				
7. PERFORMING ORGANIZATION NAME(S) AND ADDRESS(ES) Air Force Institute of Technology, WPAFB OH 45433-6583			8. PERFORMING ORGANIZATION REPORT NUMBER AFIT/GAE/ENY/95D-03	
9. SPONSORING/MONITORING AGENCY NAME(S) AND ADDRESS(ES) Steve L. Williams ASC/XR, WPAFB OH			10. SPONSORING/MONITORING AGENCY REPORT NUMBER	
11. SUPPLEMENTARY NOTES				
12a. DISTRIBUTION/AVAILABILITY STATEMENT Distribution Unlimited			12b. DISTRIBUTION CODE	
13. ABSTRACT (Maximum 200 words) This study investigated the lift, drag and pitching moment performance of a circulation control wing in the AFIT 5-ft wind tunnel. The experimental wing model was a 20 percent thick, 8.5 percent camber, partial elliptical cross-section, single blowing slot, rectangular planform wing. The aspect ratios tested were 3.99, 3.77 and 3.75. The variables in the investigation included the slot blowing rate and model configuration. The model was modified by adding a leading edge nose droop, a trailing edge splitter plate and wing tip fences to improve flow at the leading edge, reduce separation effects, and encourage attached flow on the upper surface, respectively. Results showed increased lift due to the splitter plate at low blowing rates. The leading edge nose droop increased the stall angle of attack of the wing model as blowing was increased. The wing tip fences increased the lift coefficient at medium and high blowing rates.				
14. SUBJECT TERMS High Lift Aerodynamics, Circulation Control, Subsonic Experimental Aerodynamics			15. NUMBER OF PAGES 96	
			16. PRICE CODE	
17. SECURITY CLASSIFICATION OF REPORT UNCLASSIFIED	18. SECURITY CLASSIFICATION OF THIS PAGE UNCLASSIFIED	19. SECURITY CLASSIFICATION OF ABSTRACT UNCLASSIFIED	20. LIMITATION OF ABSTRACT UL	

GENERAL INSTRUCTIONS FOR COMPLETING SF 298

The Report Documentation Page (RDP) is used in announcing and cataloging reports. It is important that this information be consistent with the rest of the report, particularly the cover and title page. Instructions for filling in each block of the form follow. It is important to ***stay within the lines*** to meet ***optical scanning requirements***.

Block 1. Agency Use Only (Leave blank).

Block 2. Report Date. Full publication date including day, month, and year, if available (e.g. 1 Jan 88). Must cite at least the year.

Block 3. Type of Report and Dates Covered. State whether report is interim, final, etc. If applicable, enter inclusive report dates (e.g. 10 Jun 87 - 30 Jun 88).

Block 4. Title and Subtitle. A title is taken from the part of the report that provides the most meaningful and complete information. When a report is prepared in more than one volume, repeat the primary title, add volume number, and include subtitle for the specific volume. On classified documents enter the title classification in parentheses.

Block 5. Funding Numbers. To include contract and grant numbers; may include program element number(s), project number(s), task number(s), and work unit number(s). Use the following labels:

C - Contract	PR - Project
G - Grant	TA - Task
PE - Program Element	WU - Work Unit Accession No.

Block 6. Author(s). Name(s) of person(s) responsible for writing the report, performing the research, or credited with the content of the report. If editor or compiler, this should follow the name(s).

Block 7. Performing Organization Name(s) and Address(es). Self-explanatory.

Block 8. Performing Organization Report Number. Enter the unique alphanumeric report number(s) assigned by the organization performing the report.

Block 9. Sponsoring/Monitoring Agency Name(s) and Address(es). Self-explanatory.

Block 10. Sponsoring/Monitoring Agency Report Number. (If known)

Block 11. Supplementary Notes. Enter information not included elsewhere such as: Prepared in cooperation with...; Trans. of...; To be published in.... When a report is revised, include a statement whether the new report supersedes or supplements the older report.

Block 12a. Distribution/Availability Statement. Denotes public availability or limitations. Cite any availability to the public. Enter additional limitations or special markings in all capitals (e.g. NOFORN, REL, ITAR).

DOD - See DoDD 5230.24, "Distribution Statements on Technical Documents."

DOE - See authorities.

NASA - See Handbook NHB 2200.2.

NTIS - Leave blank.

Block 12b. Distribution Code.

DOD - Leave blank.

DOE - Enter DOE distribution categories from the Standard Distribution for Unclassified Scientific and Technical Reports.

NASA - Leave blank.

NTIS - Leave blank.

Block 13. Abstract. Include a brief (*Maximum 200 words*) factual summary of the most significant information contained in the report.

Block 14. Subject Terms. Keywords or phrases identifying major subjects in the report.

Block 15. Number of Pages. Enter the total number of pages.

Block 16. Price Code. Enter appropriate price code (*NTIS only*).

Blocks 17. - 19. Security Classifications. Self-explanatory. Enter U.S. Security Classification in accordance with U.S. Security Regulations (i.e., UNCLASSIFIED). If form contains classified information, stamp classification on the top and bottom of the page.

Block 20. Limitation of Abstract. This block must be completed to assign a limitation to the abstract. Enter either UL (unlimited) or SAR (same as report). An entry in this block is necessary if the abstract is to be limited. If blank, the abstract is assumed to be unlimited.